# Technical Report

TR-2016-009

**Hierarchical Model Reduction for Incompressible Flows in Cylindrical Domains: The Axisymmetric Case**

by

Sofia Guzzetti, Simona Perotto, Alessandro Veneziani

Mathematics and Computer Science

**EMORY UNIVERSITY**

INTERNATIONAL JOURNAL FOR NUMERICAL METHODS IN ENGINEERING
*Int. J. Numer. Meth. Engng* 0000; **00**:1–**??**
Published online in Wiley Online Library (wileyonlinelibrary.com). DOI: 10.1002/nme

# Hierarchical Model Reduction for Incompressible Flows in Cylindrical Domains: The Axisymmetric Case

Sofia Guzzetti[1]* Simona Perotto[2] and Alessandro Veneziani[1]

[1] *Department of Mathematics & Computer Science, Emory University, USA*
[2] *MOX, Department of Mathematics, Politecnico di Milano, Italy*

SUMMARY

*Hierarchical Model (HiMod) Reduction* provides an efficient way to solve Partial Differential Equations in domains with a geometrically dominant direction, like slabs or pipes. The associated solution is regarded as the combination of mainstream dynamics driven by the geometry and transverse components. The latter are generally of secondary importance so to be described by few degrees of freedom of a spectral approximation introduced at the top of a finite element discretization of the mainstream. Thus, the 3D nature of the problem is broken into a basically 1D description added by transverse details. The versatility of this approach is that the accuracy of the method can be adaptively refined when needed, by judiciously selecting the number of transverse modes - as opposed to purely 1D models popular in computational hemodynamics and gasdynamics. After having investigated the basic features of the method in slab-like domains - where the Cartesian tensor product framework facilitates the practical implementation, in this paper we consider cylindrical pipes with polar coordinates. The selection of a different coordinate system rises several issues in particular for the most appropriate selection of the modal basis functions. Having computational hemodynamics as reference application, we address here the HiMod approximation of Advection-Diffusion-Reaction as well as Incompressible Navier-Stokes equations in axisymmetric domains.


Received . . .

KEY WORDS: Internal Incompressible Fluid Dynamics; Model Reduction; Finite Elements; Spectral Methods; Cylindrical Domains

## 1. INTRODUCTION AND BACKGROUND

*Hierarchical Model (HiMod) Reduction* is a method proposed in [1] for the efficient solution of Partial Differential Equations defined in domains with a geometrically dominant direction, like slabs or pipes. In the spirit of a separation of variables, the HiMod solution is regarded as the combination of mainstream dynamics driven by the geometry and transverse components. The latter are generally of secondary importance so to be described by few degrees of freedom of a spectral approximation introduced along the transverse direction in combination with a finite element discretization of the mainstream. Thus, the original 3D problem commutes into a system of coupled one-dimensional problems. The power of this technique lies in its hierarchical nature, so that a numerical 1D solution can be easily expanded towards the three-dimensional original domain thanks to the modal basis. If the size of the modal basis is chosen in a proper way along the mainstream (see [2]), the transverse dynamics can be reliably approximated. Transverse dynamics would be otherwise dropped by purely 1D models, like the ones used in computational hemodynamics or gasdynamics [3, 4].

*Correspondence to: 400 Dowman Dr NE, 30322 Atlanta (GA) USA E-mail:sofia.guzzetti@emory.edu

HiMod reduction has been employed to solve Advection-Diffusion-Reaction (ADR) problems in two-dimensional domains (see, e.g., [1, 2, 5, 6]) and parallelepipeds [7]. Three dimensional problems are also considered in [8] for patient-specific geometries. In this work the domain is discretized through pipe-like finite elements, which are subsequently mapped to a reference square geometry where the Cartesian framework is exploited for the construction of the modal basis by tensor product. Here, we propose a formulation purposely devised for cylinder-like geometries, by polar coordinates. These coordinates are, in principle, the most suited to an effective HiMod discretization in cylindrical domains. However, the choice of the modal basis requires specific investigations, that are precisely the subject of the present paper. This work is intended to move a first step forward to real medical applications, in the perspective of a further extension of the HiMod approach to the modeling of the entire cardiovascular network (see, for example, [9, 8]).

In order to highlight the main features of HiMod reduction in cylindrical domains, in Section 2 we address the issue of the choice of a modal basis tailored to a transverse circular section. The performance of different functions is validated through suitable numerical assessments. In Section 3 we apply the method to a three-dimensional ADR problem in a cylindrical domain with circular section. On this basis, in Section 4 we move to vector problems coming from internal incompressible fluid dynamics. The generalized Stokes problem is briefly recalled and solved with a HiMod approach. In view of possible medical applications, in Section 5 we consider elementary models for arterial stenoses and aneurysms. At this stage, we work only on axisymmetric geometries. We refer to future work for an extension of HiMod to the more general non-axisymmetric case [10]. Evolution in time does not bring significant changes and it is introduced directly when presenting the numerical results. We compare the results presented here with [8] to point out the expected better properties of cylindrical coordinates in comparison with the Cartesian ones.

## 2. HIMOD IN CYLINDRICAL DOMAINS

### *2.1. The geometric setting*

Let us consider a cylindrical domain with rectilinear axis and circular section with variable radius $R$ (see Figure 1). We assume that the domain can be represented as a three-dimensional fiber bundle $\Omega = \bigcup_{x\in\Omega_{1D}} \{x\} \times \gamma_x$, where $\Omega_{1D}$ is a one-dimensional domain, and $\gamma_x \subset \mathbb{R}^2$ represents the two-dimensional fiber associated with the generic point $x \in \Omega_{1D}$ (see Figure 1). In particular, the supporting fiber is the axis, while $\gamma_x$ is the transverse section centered at $x$. The leading dynamics are aligned with $\Omega_{1D}$, whereas the transverse dynamics are parallel to fibers $\gamma_x$. For the sake of simplicity, we assume a rectilinear axis $\Omega_{1D} = ]x_0, x_1[$, but the more general case of a curved supporting fiber can be considered as well [11, 12]. For each $x \in \Omega_{1D}$, we introduce the mapping

$$\psi_x \ : \ \gamma_x \to \hat{\gamma}, \tag{1}$$

between the physical fiber $\gamma_x$ and a reference fiber $\hat{\gamma}$. We set $\hat{\mathbf{z}} = (\hat{x}, \hat{\mathbf{y}}) = \hat{\boldsymbol{\psi}}(x, \mathbf{y}) = (x, \psi_x(\mathbf{y}))$ as the image of the physical point $\mathbf{z} = (x, \mathbf{y}) \in \Omega$ through the global map $\hat{\boldsymbol{\psi}} : \Omega \to \hat{\Omega}$, where $\hat{\Omega}$ is the reference cylinder described by the coordinates $(x, \hat{\mathbf{y}})$, with $\hat{\mathbf{y}} = \psi_x(\mathbf{y}) = (\hat{r}, \hat{\vartheta}) \in [0, 1) \times [0, 2\pi]$, so that the transverse reference fiber $\hat{\gamma}$ coincides with the unit circle (see Figure 1). We assume $\psi_x$ to be a $C^1$-diffeomorphism for all $x \in \Omega_{1D}$ and $\hat{\boldsymbol{\psi}}$ to be differentiable with respect to $\mathbf{z}$.

This is not the only possible approach for representing a cylindrical domain. For instance, in [8] each elementary pipe element is mapped to a reference hexaedron. This allows using a Cartesian framework in the reference space and constructing the basis functions by tensor product. In this case, the geometric map lacks of regularity at the vertices of the hexahedron. In principle, this is not necessarily troublesome, and, in general, the Cartesian framework guarantees easiness of implementation. However, the choice of a cylindrical basis is intrinsically more tailored to the geometry of a pipe. We argue that this choice, even though more involved in practice, may lead to better accuracy and efficiency. We numerically investigate this statement in the sequel.




DOI: 10.1002/nme

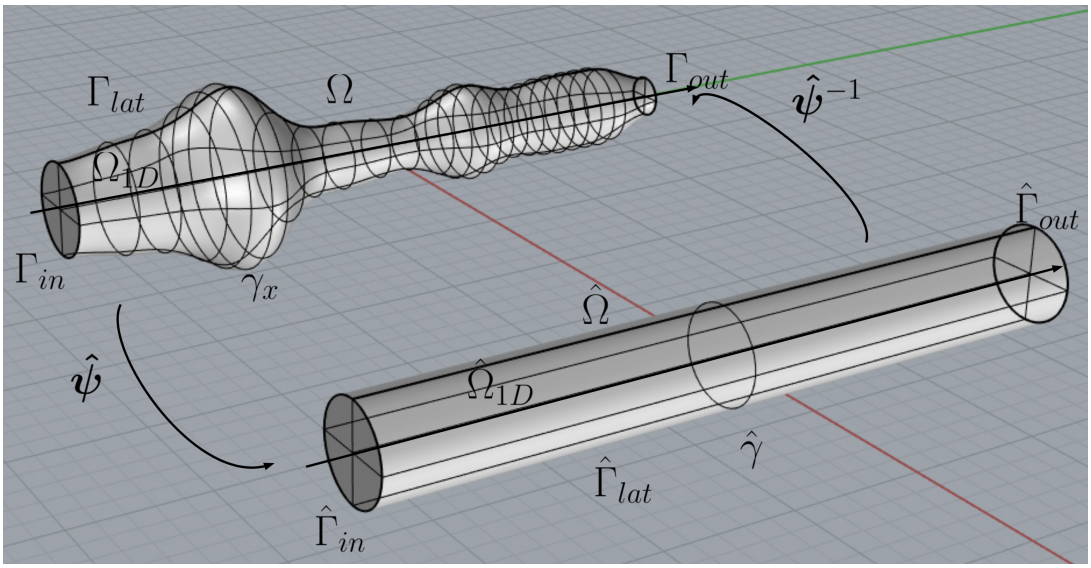


Figure 1. Sketch of the map between the physical and the reference domain.

### 2.2. *The reference basis set*

The fiber structure featured by the domain $\Omega$ has a key role in setting the HiMod reduction. We resort to different function spaces along $\Omega_{1D}$ and on the transverse fibers. The standard notation for the Sobolev spaces as well as for the spaces of functions bounded a.e. in $\Omega$ is adopted [13]. With reference to standard scalar ADR problems, we introduce the function space $V_{1D} \subseteq H^1(\Omega_{1D})$ on $\Omega_{1D}$, such that the related functions vanish on Dirichlet boundaries. On the transverse reference fiber we set a modal basis $\{\hat{\varphi}_k\}_{k\in\mathbb{N}^+} \subset H^1(\hat{\gamma})$. In particular, we select functions orthonormal with respect to a weighted scalar product in $L^2(\hat{\gamma})$. Clearly, boundary conditions on $\Gamma_{lat}$ have to be taken into account by the modal basis. Then, the discrete transverse function space is defined as $V_{\hat{\gamma}} = span\{\hat{\varphi}_k\}$. For a certain $m \in \mathbb{N}^+$, the combination of spaces $V_{1D}$ and $V_{\hat{\gamma}}$ yields the *reduced space*

$$V_m = \left\{ v_m(x,\mathbf{y}) = \sum_{k=1}^{m} \tilde{v}_k(x)\hat{\varphi}_k(\psi_x(\mathbf{y})),\ \text{with } \tilde{v}_k \in V_{1D},\ \hat{\varphi}_k \in V_{\hat{\gamma}},\ x \in \Omega_{1D},\ \mathbf{y} \in \gamma_x \right\}, \quad (2)$$

with

$$\tilde{v}_k(x) = \int_{\hat{\gamma}} v_m(x, \psi_x^{-1}(\hat{\mathbf{y}}))\hat{\varphi}_k(\hat{\mathbf{y}})d\hat{\gamma} \qquad k \in \{1,\dots,m\}, \quad (3)$$

thanks to the orthonormality of the basis. There are several possibilities for constructing a modal basis in polar coordinates. In a "Top-Down" approach, the basis function set for the coordinate system $\hat{\mathbf{y}} = (\hat{r}, \hat{\vartheta})$ descends from the solution to an eigenvalue/eigenfunction procedure - as opposed to a "Bottom-Up" approach, where the basis is assembled for coordinates $\hat{r}$ and $\hat{\vartheta}$, separately. We discuss these two options hereafter.

#### 2.2.1. *The Top-Down approach*

As advocated in [7], a possible strategy to build the modal basis is to solve an auxiliary *Sturm-Liouville* eigenvalue problem (see, for example, [14, 15, 16]) on the transverse section,

$$\begin{cases} \mathcal{L}\hat{\varphi}_k = \hat{\lambda}_k w \hat{\varphi}_k & \text{in } \hat{\gamma} \\ BC & \text{on } \partial\hat{\gamma}, \end{cases} \quad (4)$$



DOI: 10.1002/nme

| BC type | Condition | Functor |
|---|---|---|
| Dirichlet | $\hat{\varphi}_k = 0$ | $J_n(\sqrt{\hat{\lambda}_j})$ |
| Neumann | $\mu \nabla \hat{\varphi}_k \cdot \mathbf{n} = 0$ | $\frac{\sqrt{\hat{\lambda}_j}}{R} J_n'(\sqrt{\hat{\lambda}_j})$ |
| Robin | $\mu \nabla \hat{\varphi}_k \cdot \mathbf{n} + \chi \hat{\varphi}_k = 0$ | $\frac{\sqrt{\hat{\lambda}_j}}{R} J_n'(\sqrt{\hat{\lambda}_j}) + \frac{\chi}{\mu} J_n(\sqrt{\hat{\lambda}_j}) \quad (\mu, \chi > 0)$ |

Table I. Functors associated with different types of boundary conditions.

so to include in an essential way the boundary conditions (of any type) in the basis, where $\mathcal{L}$ is a suitable differential operator, $(\hat{\lambda}_k, \hat{\varphi}_k)$ denotes a corresponding eigenpair, and $w$ is a positive continuous weight function. If the bilinear form associated with the weak formulation of (4) satisfies the hypotheses of the Spectral Theorem [15], the eigenfunctions associated with the operator $\mathcal{L}$ are orthogonal with respect to the $L^2_w$-weighted scalar product and form a complete set in the same space. Since functions $\hat{\varphi}_k$ automatically include the lateral boundary conditions, the set $\{\hat{\varphi}_k\}$ has been called "educated" basis [7].

**Scalar problems** Let $\mathcal{L}$ in (4) be the Laplace operator on the reference unit circle in polar coordinates. With this operator, we associate the set of eigenfunctions

$$\hat{\varphi}_{j,n}\left(\hat{r}, \hat{\vartheta}\right) = \frac{1}{\sqrt{2\pi}\|J_n\|_{L^2_w(0,1)}} \left(\sin(n\hat{\vartheta}) + \cos(n\hat{\vartheta})\right) \; J_n\left(\sqrt{\hat{\lambda}_j}\hat{r}\right), \tag{5}$$

where $J_n$ is the Bessel function of first type of order $n \in \mathbb{N}^+$ [14, 17, 18, 19]. In particular, the frequency $\sqrt{\hat{\lambda}_j}$ is the $j$-th root of $J_n$. More in general, for each type of constraint (Dirichlet/Neumann/Robin), $\hat{\lambda}_j$ is obtained as the (squared) $j$-th root of a specific functor (see Table I). As a result, the ordering of the basis functions $\{\hat{\varphi}_k\}$ depends on the two indices $j$ and $n$, i.e., $k = k(j, n)$ (for more details, see [20]).

**Vector problems** In view of hemodynamic applications, hereafter we construct a modal basis by solving problem (4) completed with homogeneous Dirichlet boundary conditions. Moreover, the operator $\mathcal{L}$ is chosen as the Stokes operator on the unit disk. Following the procedure adopted for scalar problems, the corresponding eigenfunctions for the pressure and for the velocity are computed as in [21]. Thus, for $n \neq 0$, they read as

$$\begin{aligned} &p_n(\hat{r}) = c_1 \hat{r}^n, \\ &\mathbf{u}_{j,n}(\hat{r}, \hat{\vartheta}) = c_1 \exp(in\hat{\vartheta}) \begin{bmatrix} \dfrac{n}{\hat{\lambda}_j}\hat{r}^{n-1} - \dfrac{nJ_n\left(\sqrt{\hat{\lambda}_j}\hat{r}\right)}{\hat{r}\hat{\lambda}J_n\left(\sqrt{\hat{\lambda}_j}\right)} \\ in\left(\dfrac{\hat{r}^{n-1}}{\hat{\lambda}_j} - \dfrac{J_{n-1}\left(\sqrt{\hat{\lambda}_j}\hat{r}\right) - J_{n+1}\left(\sqrt{\hat{\lambda}_j}\hat{r}\right)}{2n\sqrt{\hat{\lambda}_j}J_n\left(\sqrt{\hat{\lambda}_j}\right)}\right) \end{bmatrix}, \end{aligned} \tag{6}$$

respectively, where $\sqrt{\hat{\lambda}_j}$ runs through all the roots of $J_{n+1}$, and the coefficient $c_1$ is determined via the unitary norm constraint. Although from a theoretical viewpoint functions $p_n$ and $\mathbf{u}_{j,n}$ are tailored to the problem we aim to solve, from a practical perspective there are some drawbacks. Specifically, we need here to drop the complex part, with a relevant loss of details. More in general (for both scalar and vector problems), Bessel functions are extremely sensitive to numerical errors [22, 19, 23, 24, 25, 16] and this may limit their use.




DOI: 10.1002/nme

*2.2.2. The Bottom-Up approach*

As an alternative to the Top-Down approach, a two-step procedure is proposed in [24]. A classic Fourier expansion for the angular variable is first adopted and, subsequently, a radial basis $\{\xi_n(\hat{r})\}_{n=0}^{\infty}$ is introduced to reproduce the $\hat{r}$-dependent Fourier coefficients. Thus, the expansion of an arbitrary function $f \in L^2_w([0,1] \times [0,2\pi))$ reads

$$f(\hat{r},\hat{\vartheta}) = \sum_{j=0}^{\infty}\sum_{n=0}^{\infty}\Big[f_{jn}\xi_n(\hat{r})\cos(j\hat{\vartheta}) + g_{jn}\xi_n(\hat{r})\sin(j\hat{\vartheta})\Big], \tag{7}$$

with $f_{jn},\ g_{jn} \in \mathbb{R}$ for any $j,n \in \mathbb{N}^+$. This means solving two uncoupled 1D Sturm-Liouville eigenvalue problems, one for the angular and one for the radial component, respectively. Then, the 2D basis is given by

$$\hat{\varphi}^{\sin,\cos}_{j,n}(\hat{r},\hat{\vartheta}) = \xi_n(\hat{r})\begin{cases}\cos(j\hat{\vartheta})\\ \sin(j\hat{\vartheta}),\end{cases} \tag{8}$$

where the superscript sin/cos specifies the type of trigonometric function considered and $n = n(j)$, with $j,n \in \mathbb{N}^+$. As in the previous case, the ordering of the basis functions $\{\hat{\varphi}_k\}$ depends on the two indices $j$ and $n$, i.e., $k = k(j,n)$ [20]. It is important to point out that, depending on the selected radial basis $\{\xi_n\}$, some suitable manipulations may be required to enforce Dirichlet boundary conditions in an essential way, since the basis (8) is not "educated". Furthermore, this technique leads to some complications for the hierarchical ordering of the spectrum. Since no 2D eigenvalue problem is defined, there does not exist any hierarchy between the $r$-eigenvalues and the $\vartheta$-eigenvalues, and the corresponding eigenfunctions. Hence, the selection of the number of radial modes and of trigonometric functions is somehow arbitrary. Two criteria are proposed in [24], namely *rectangular* and *triangular* truncations. The former employs the same number of radial functions for each angular wave number $j$. The latter decreases the number of radial basis functions as $j$ increases, until the highest wave number has a single radial basis function. This criterion is usually employed for spherical harmonics because it guarantees the property of "equiareal resolution". Nevertheless, such property is not guaranteed in a cylindrical setting. Therefore, in the following we adopt a rectangular truncation, which is beneficial in terms of implementation. Smoothness properties are guaranteed by the Parity Theorem, that rules the combination of radial and trigonometric components in the construction of a polar modal basis. We provide the corresponding statement for completeness [24].

*Theorem* (*Coordinates: Parity in Radius)*
Let $f$ be a function analytic in $r = 0$, expanded by a Fourier series in $\vartheta$ as

$$f(r,\vartheta) = \sum_{j=0}^{\infty}\left[f_j(r)\cos(j\vartheta) + g_j(r)\sin(j\vartheta)\right].$$

Continuity of function $f$ and of its derivatives requires $f_j(r)$ and $g_j(r)$ to have $j$-th order zeros at $r = 0$. In addition, if $j$ is even, then $f_j(r)$ and $g_j(r)$ are both symmetric about $r = 0$ and the corresponding power series contain only even powers of $r$. If $j$ is odd, then $f_j(r)$ and $g_j(r)$ are both antisymmetric about $r = 0$ and the associated power series contain only odd powers of $r$.

It follows that, to ensure the regularity of series (7), it suffices that odd powers of $r$ are paired only with $\cos(j\vartheta)$ and $\sin(j\vartheta)$ where $j$ is odd, and conversely. Different possible choices for radial basis sets from [24, 26] are shown in Table II and discussed below. Figure 2 (left) shows the performance of different basis sets in approximating the function $f(\hat{r}) = \cos(\frac{\pi}{2}\hat{r})$ on the interval $[0,1]$. The relative error is defined as $e = \|f - f_{approx}\|_{L^2_w(\Omega)}/\|f\|_{L^2_w(\Omega)}$, where $w(\hat{r}) = \hat{r}$ and $f_{approx}$ denotes the approximation of $f$ via the truncation of (7). For the sake of completeness, we discuss several possible choices of basis functions.

**Bessel functions: $J_n(\lambda_j\hat{r})$.** The modal coefficients of Bessel series asymptotically behave like $1/j^3$ [25, 22]. For this reason Bessel functions are expected to be a bad choice for function




DOI: 10.1002/nme

| Family | $\xi_n(\hat{r})$, $n = n(j)$ | parameters |
|---|---|---|
| Bessel | $J_n(\lambda_j \hat{r})$ | $\lambda_j$: the $j$-th root of $J_n(\hat{r})$ |
| Robert | $\hat{r}^j T_n(\hat{r})$ | $T_n$: Chebyshev polynomial of degree $n$ |
| Chebyshev-linear shift | $T_n(2\hat{r} - 1)$ | $T_n$: Chebyshev polynomial of degree $n$ |
| Chebyshev-quadratic shift | $T_n(2\hat{r}^2 - 1)$ | $T_n$: Chebyshev polynomial of degree $n$ |
| Jacobi | $\hat{r}^j P^{0,j}_{\frac{n-j}{2}}(2\hat{r}^2 - 1)$ | $P^{0,j}_h$: Jacobi polynomial of degree $h$ and order $(0, j)$ |

Table II. Main families of eigenfunctions $\xi_n$ for a 1D Sturm-Liouville eigenvalue problem in the radial coordinate. Note that the ordering of such basis may depend on the ordering of the angular basis.

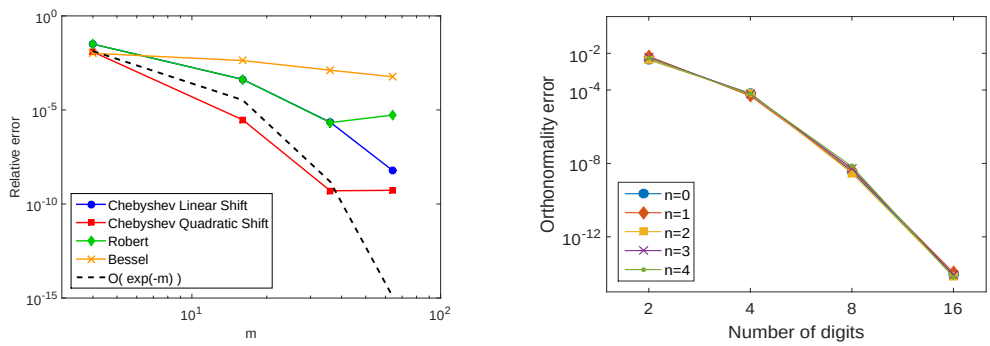


Figure 2. Left: Relative error for the approximation of the function $f(\hat{r}) = \cos\left(\frac{\pi}{2}\hat{r}\right)$ with Chebyshev polynomials with linear (●) and quadratic (■) shift, Robert (♦) and Bessel ($\times$) functions. An exponential decay is shown by the dashed line. Right: Orthonormality error associated with the basis functions $J_n(\lambda_j \hat{r})$, for $n = 0, 1, \ldots, 4$, $j = 1, 2, \ldots, 8$, as a function of the numerical precision expressed in number of digits.

approximation. For instance, Figure 2 (left) shows that even a large number of modes is unable to guarantee a desired accuracy on the relative error. Moreover, this basis is highly sensitive to numerical precision. The plot in Figure 2 (right) shows that the basis functions lose orthonormality as the accuracy of the roots $\lambda_j$ decreases. The orthonormality error associated with the basis functions $J_n(\lambda_j \hat{r})$, for $n = 0, 1, \ldots, 4$, $j = 1, 2, \ldots, 8$, is measured via the Frobenius norm of the matrix $M_n - I$, where $M_n$ is the mass matrix associated with the normalized Bessel functions of order $n$, with components $[M_n]_{jl} = \|J_n(\lambda_j \hat{r})\|^{-1}_{L^2_w(0,1)} \|J_n(\lambda_l \hat{r})\|^{-1}_{L^2_w(0,1)} \int_0^1 J_n(\lambda_j \hat{r}) J_n(\lambda_l \hat{r}) \hat{r} d\hat{r}$, and $I$ is the identity matrix.

**Polar Robert functions:** $\hat{r}^j T_n(\hat{r})$**.** As addressed in [24, 26], this basis is extremely ill-conditioned. Indeed, in proximity of $\hat{r} = 1$, the linear independence of the low-degree basis functions is compromised, since the variation of these functions in this region is so slow that they are asymptotically equivalent [26]. These features make the polar Robert functions a basis unsuitable in most cases.

**Shifted-Chebyshev polynomials with linear argument:** $T_n(2\hat{r} - 1)$**.** The grid $\{\hat{r}_i\}_{i=0}^N$ constituted by the roots of the Shifted-Chebyshev polynomial of order $(N + 1)$ has points clustered near both $\hat{r} = 0$ and $\hat{r} = 1$. this property makes this grid ideal to solve large gradients near the origin, but less suited to a generic dependence of the function at hand on the radial coordinate.



DOI: 10.1002/nme

**Shifted-Chebyshev polynomials with quadratic argument:** $T_n(2\hat{r}^2-1)$**.** In order to satisfy the Parity Theorem, the 2D basis functions are chosen so that the radial part is $\xi_n(\hat{r}) = T_n(2\hat{r}^2-1)$ if the angular index $j$ is even, $\xi_n(\hat{r}) = \hat{r}\ T_n(2\hat{r}^2-1)$ otherwise. As shown in [24], the convergence rate associated with this basis is higher with respect to the convergence guaranteed by the linear-shifted polynomials.

**One-sided Jacobi basis:** $\hat{r}^j P^{0,j}_{\frac{n-j}{2}}(2\hat{r}^2-1)$**.** The basis set consisting of Jacobi polynomials is very similar to the one associated with Robert functions. Indeed, it is represented by Jacobi polynomials, scaled by the factor $\hat{r}^j$ (see Table II). Unlike Robert functions, thanks to the orthogonality constraint, these polynomials oscillate mostly near $\hat{r}=1$ and consequently the roots move closer and closer to the outer boundary for a fixed degree and by increasing $j$.

Based on the above discussion on the distinguishing features of each family of functions, the shifted Chebyshev polynomials with quadratic argument are selected as the modal basis for the numerical assessment. Indeed, they feature good conditioning properties, and they guarantee an accurate representation of the approximated function and a fast convergence of the corresponding modal expansion.

## 3. HIMOD IN CYLINDRICAL DOMAINS FOR SCALAR ADVECTION-DIFFUSION-REACTION PROBLEMS

As a first benchmark, we apply the HiMod technique to the following linear ADR problem:

$$\begin{cases} -\nabla\cdot(\mu\nabla u) + \mathbf{b}\cdot\nabla u + \sigma u = f & \text{in } \Omega \\ u = u_{in} & \text{on } \Gamma_{in} \\ \mu\nabla u\cdot\mathbf{n} = 0 & \text{on } \Gamma_{out} \\ u = 0 & \text{on } \Gamma_{lat}, \end{cases} \tag{9}$$

where $\Omega$ is a cylinder of length $L_x$ and radius $R$, and the boundary is defined as in Figure 1. Let $\mu, \sigma \in L^\infty(\Omega)$, with $\mu \geq \mu_0 > 0$ a.e. in $\Omega$, be the diffusivity and the reaction coefficient, respectively, and $\mathbf{b} = (b_x, b_r, b_\vartheta)^T \in [L^\infty(\Omega)]^3$ the convective field. We assume $\nabla\cdot\mathbf{b} \in L^\infty(\Omega)$ such that $-\frac{1}{2}\nabla\cdot\mathbf{b} + \sigma \geq 0$ a.e. in $\Omega$, and $f \in L^2(\Omega)$ so to guarantee the well-posedness of the weak form of the problem.

We set the problem on the space $V_m$ defined in (2). Hypotheses of *conformity* and *spectral approximability* are required to guarantee the well-posedness of the reduced problem and the convergence to the full problem [1].

We introduce a (uniform) partition $\mathcal{T}_h$ of $\Omega_{1D}$ and the corresponding finite element space $V^h_{1D} \subset V_{1D}$, with $\dim(V^h_{1D}) = N_h$ and basis $\{\zeta_l\}_{l=1}^{N_h}$, such that a standard density hypothesis of $V^h_{1D}$ in $V_{1D}$ is guaranteed. The discrete counterpart of (2) reads as

$$V^h_m = \left\{ v^h_m(x,\mathbf{y}) = \sum_{k=1}^m \tilde{v}^h_k(x)\hat{\varphi}_k(\psi_x(\mathbf{y})),\ \text{with } \tilde{v}^h_k \in V^h_{1D},\ \hat{\varphi}_k \in V_{\hat{\gamma}},\ x \in \Omega_{1D},\ \mathbf{y} \in \gamma_x \right\}. \tag{10}$$

Then, the HiMod approximation $u^h_m \in V^h_m$ for (9) and the corresponding test function $v^h_m \in V^h_m$ read as $u^h_m(x,\mathbf{y}) = \sum_{k=1}^m \sum_{i=1}^{N_h} u_{k,i}\zeta_i(x)\hat{\varphi}_k(\psi_x(\mathbf{y}))$ and $v^h_m(x,\mathbf{y}) = \zeta_l(x)\hat{\varphi}_j(\psi_x(\mathbf{y}))$, respectively, for any $l = 1,\dots,N_h$ and any $j = 1,\dots,m$. Thus, the discrete HiMod formulation becomes:

For $k = 1,\dots,m$ and $i = 1,\dots,N_h$, find $u_{k,i} \in \mathbb{R}$ such that, for any $j = 1,\dots,m$, $l = 1,\dots,N_h$

$$\sum_{k=1}^m \sum_{i=1}^{N_h} \int_{\hat{\Omega}_{1D}} \left\{ \mathfrak{d}_{kj}\ \zeta_i'\zeta_l' + \mathfrak{c}_{kj}\ \zeta_i'\zeta_l + \mathfrak{b}_{kj}\ \zeta_i\zeta_l' + \mathfrak{a}_{kj}\ \zeta_i\zeta_l \right\} u_{k,i}\, d\hat{x} = \int_{\hat{\Omega}_{1D}} \mathfrak{f}_j\zeta_l\, d\hat{x}, \tag{11}$$




DOI: 10.1002/nme

where coefficients $\{\mathfrak{a}, \mathfrak{b}, \mathfrak{c}, \mathfrak{d}\}_{kj}$, $\{\mathfrak{f}\}_j$ collect the contribution of the dynamics transverse to $\hat{\Omega}_{1D}$ (we refer to Appendix A for an explicit expression of such coefficients). Problem (11) represents a linear system of $m$ coupled 1D problems, characterized by an $mN_h \times mN_h$ block matrix $A$ (with a hierarchical structure that we point out in Section 4). The indices $j$ and $k$, associated with the modes, identify the macro-structure of $A$ (they run on the block rows and block columns, respectively), whereas $l$ and $i$, related to the finite element basis, identify the rows and the columns of each block, respectively. Each $N_h \times N_h$ block $A_{jk}$ preserves the sparsity pattern peculiar of the adopted 1D finite element approximation.

The rationale of HiMod is that a small modal index $m$ is expected to be enough to reliably approximate the transverse dynamics, so that solving (11) requires dealing with a small number of coupled 1D problems. As for a back-of-the-envelope calculation, for a three-dimensional problem set on a cylindrical domain discretized with a structured grid via P1-FE, the degrees of freedom are $N_x N_r N_\vartheta$, being $N_x$, $N_r$ and $N_\vartheta$ the number of degrees of freedom in the $x$, $r$ and $\vartheta$ dimension, respectively. With a HiMod reduction the number of unknowns is $mN_x$. Then, if $m \ll N_r N_\vartheta$, the resulting matrix is much smaller compared to the one associated with the full problem. More accuracy is attained by properly adjusting $m$. So HiMod can be regarded at the baseline as a versatile 1D approximation that can be properly (and locally) enhanced.

### *3.1. Numerical Assessment*

In order to validate the method, we test HiMod on the basis functions (5) obtained with the Top-Down approach for different types of boundary conditions.* Functions (8) will be tested in the sequel. We consider a case where the analytical solution is known to investigate the error behavior, and a more realistic test whose analytical solution is not available. In the latter case, the ground truth solution is provided by the standard $\mathbb{P}^1$-Finite Element method (FEM) associated with a very fine grid.

#### *3.1.1. Convergence analysis*

Let us consider problem (9) with $L_x = 5$, $R = 1$, $\mu = 1$, $b_x = 5$, $b_r = 0$, $b_\vartheta = 0$, $\sigma = 10$. The forcing term and the boundary conditions on $\Gamma_{in}$ are adjusted to have three different analytical solutions, i.e.,

$$u_{R2}(x, r, \vartheta) = (R^2 - r^2)(L_x - x)^2, \tag{12a}$$

$$u_{R3}(x, r, \vartheta) = -\frac{1}{4}r^2 + \frac{1}{6}r^3 + \frac{1}{12}, \tag{12b}$$

$$u_{R4}(x, r, \vartheta) = (R^2 - r^2)^2(L_x - x)^2. \tag{12c}$$

**Dirichlet BC** Figure 3 (left) shows the trend of the $L^2(\Omega)-$norm of the HiMod error, $u_{R2} - u_m^h$, for different values of $h$ and $m$ for the exact solution (12a). The global error takes into account both the 1D finite element discretization and the modal error. For a fixed value of $h$ and for $m$ large enough, the error stagnates, since the FEM error dominates the total error. Conversely, for small values of $h$, the error is dominated by the modal component. The convergence rate is linear with respect to the reciprocal of the number of modes. This is consistent with the results in [7] on slabs. HiMod is sensibly competitive with respect to the standard FEM in terms of accuracy. For a given number of degrees of freedom (DOF), the HiMod error is about one order of magnitude lower than the FEM error (see Figure 3 (right)). Note that for $\mathbb{P}^1$-FEM the number of DOF coincides with the number of vertices of the mesh, whereas for HiMod it is given by the number of FE nodes along $\Omega_{1D}$ multiplied by the number of modes. Conversely, the number of DOF to obtain a desired tolerance is consistently smaller for the HiMod method than for FEM.

*All the experiments in this work have been performed using a C++ solver on a Dell Inspiron 15R SE 7520 equipped with a 2.10GHz Intel Core i7 processor and 8GB of RAM.




DOI: 10.1002/nme

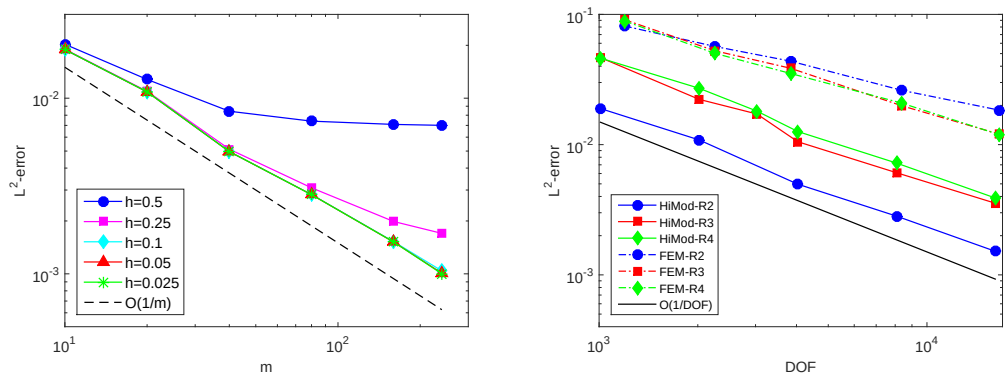


Figure 3. ADR with Dirichlet BC: $L^2(\Omega)$-norm of the HiMod error as a function of $h$ and $m$ (left); Comparison between HiMod and FEM error for different exact solutions (right).

**Neumann and Robin BC** Consider problem (9) completed with the homogeneous Robin data $\mu\nabla u \cdot \mathbf{n} + \chi u = 0$ on $\Gamma_{lat}$. For $\mu = 1$, $\chi = 1$ the analytical solution is (12c). Figure 4 (right) shows that the HiMod error decays as $O(N^{-1.5})$, being $N$ the number of DOF. The same happens for $\chi = 0$, when the Robin boundary condition reduces to a Neumann constraint, and the exact solution is (12b) (see Figure 4 (left)). Indeed, as noted in [7] for a slab, in the particular case of Neumann boundary data, an infinitely regular function whose odd derivatives vanish at the boundary is approximated by Fourier truncated series with spectral accuracy. This justifies the superconvergent trend. As for Dirichlet BC, HiMod is more accurate of approximately one order of magnitude compared with FEM.

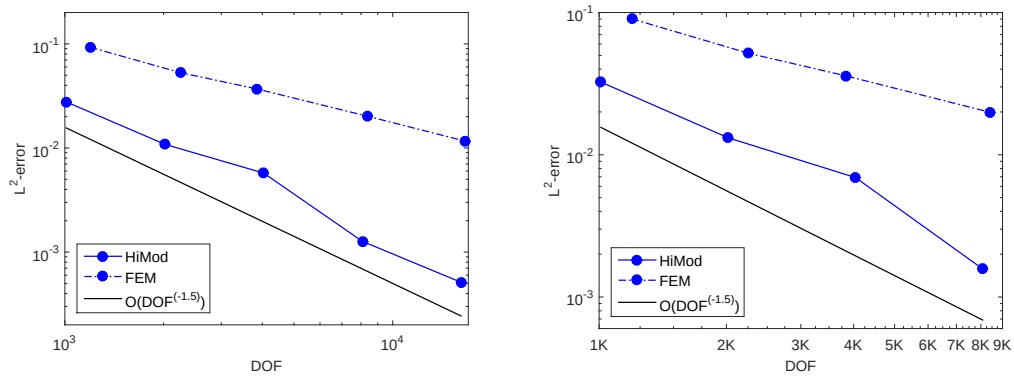


Figure 4. ADR with Neumann (left) and Robin (right) BC: $L^2(\Omega)$-norm of the HiMod error as a function of the number of DOF.

### *3.1.2. Drug release modeling*

We aim at modeling a drug-eluting stent deployed in a blood vessel. Stents are medical devices that are used in the surgical treatment of constricted arteries. They are inserted into the vessel in order to expand the lumen to prevent or alleviate an obstruction. In particular, drug-eluting stents slowly release a drug to inhibit cell proliferation, so to avoid a vascular remodeling [27].

This test case describes the effects of an advective field on a local source term. Consider problem (9) on the same domain as in the previous test, with $u_{in} = R^2 - r^2$ and a homogeneous Neumann condition on $\Gamma_{out}$. The physical parameters are set to $\mu = 1$, $\sigma = 0$, $b_x = 5$, $b_r = 0$, $b_\vartheta = 0$, while the forcing term is designed to model the presence of a high concentration $c$ of drug in proximity of




DOI: 10.1002/nme

the wall, i.e.,

$$f(x,r,\vartheta) = c\,\mathbb{1}_{\left[\frac{L_x}{7},\,\frac{L_x}{3}\right]}(x)\cdot\mathbb{1}_{\left[\frac{7}{10}R,\,R\right]}(r), \tag{13}$$

where $\mathbb{1}_{[a,b]}$ denotes the characteristic function associated with the generic interval $[a,b]$ (see Figure 5). The mesh size along $\Omega_{1D}$ and the number of modes is set to $h = 0.05$ and $m = 40$, respectively. Since this test case has no analytical solution, we refer to a FE approximation computed on a fine mesh (of approximately $97K$ nodes). A qualitative comparison between the two panels in Figure 6 shows the reliability of the HiMod procedure from a qualitative viewpoint.

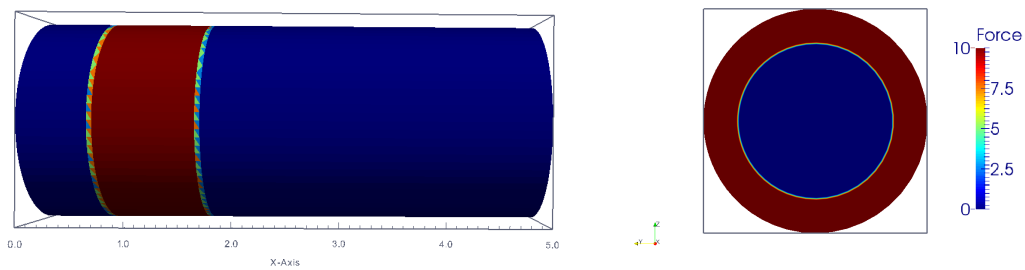


Figure 5. Forcing term modeling a drug-eluting stent: longitudinal view (left) and transverse section along the $yz$-plane (right).

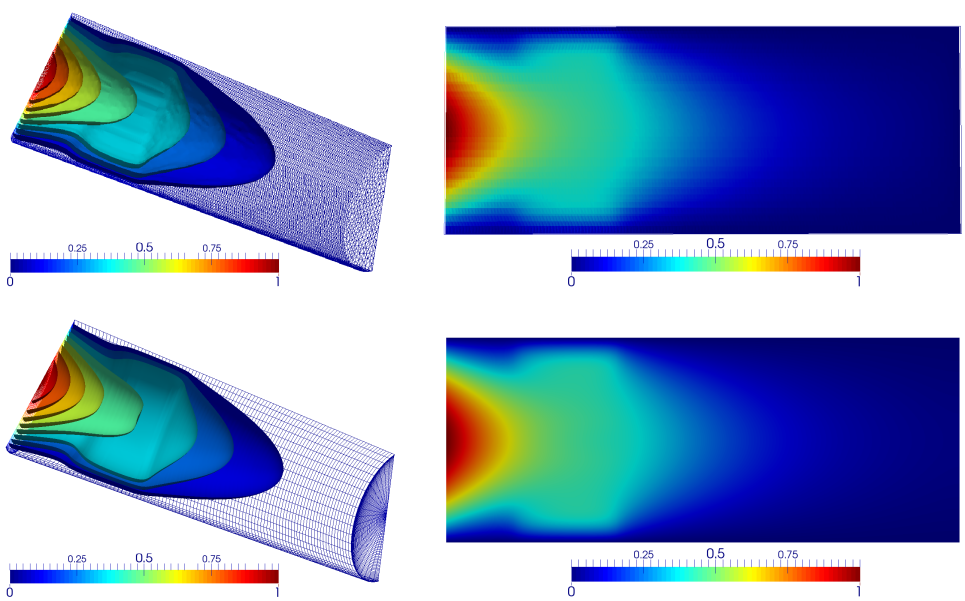


Figure 6. Drug-release modeling: FEM (top) and HiMod (bottom) solution; Contour surfaces (left) and longitudinal section (right) along the $xy$-plane.




DOI: 10.1002/nme

## 4. HIMOD IN CYLINDRICAL DOMAINS FOR THE GENERALIZED STOKES EQUATIONS

We extend the HiMod procedure to the generalized Stokes problem

$$\begin{cases} -\nabla\cdot\big(2\nu\mathbb{D}(\mathbf{u})\big)+\alpha\mathbf{u}+\nabla p=\mathbf{f} & \text{in } \Omega \\ \nabla\cdot\mathbf{u}=0 & \text{in } \Omega \\ \mathbf{u}=\mathbf{0} & \text{on } \Gamma_{lat} \\ \mathbf{u}=\mathbf{u}_0 & \text{on } \Gamma_{in} \\ (2\nu\mathbb{D}-p\mathbb{I})\mathbf{n}\cdot\mathbf{n}=0 & \text{on } \Gamma_{out}, \end{cases} \tag{14}$$

where $\alpha\geq 0$ and the kynematic viscosity $\nu>0$ in $\Omega$ are given constants, $\mathbf{f}:\Omega\to\mathbb{R}^3$ is a given force per unit mass, $\mathbf{u}:\Omega\to\mathbb{R}^3$ and $p:\Omega\to\mathbb{R}$ are the velocity field and the kinetic pressure, respectively, $\mathbb{D}(\mathbf{u})$ is the strain velocity tensor and $\mathbb{I}$ is the identity tensor. The generalized Stokes problem is solved at each time step with $\alpha=O(\Delta t^{-1})$, being $\Delta t$ the time step of a finite difference discretization of the unsteady Stokes problem. For $\alpha=0$ we recover the classical Stokes problem. We consider homogeneous Dirichlet conditions on the lateral boundary $\Gamma_{lat}$, and Dirichlet and Neumann conditions on $\Gamma_{in}$ and $\Gamma_{out}$, respectively. We will denote by $\Gamma_{dir}$ the whole portion of the boundary where Dirichlet conditions are enforced.

### *4.1. The HiMod formulation*

We formulate the weak form of problem (14) in the Sobolev spaces $V=[H^1_{\Gamma_{dir}}(\Omega)]^3$, $Q=L^2(\Omega)$, where $H^1_{\Gamma_{dir}}(\Omega)$ denotes the set of the functions in $H^1(\Omega)$ that fulfil Dirichlet conditions on $\Gamma_{dir}$. The spaces $V$ and $Q$ are endowed with a modal basis $\{\hat{\boldsymbol{\varphi}}_{u,k}\}_{k\in\mathbb{N}^+}\subset[H^1_0(\hat{\gamma})]^3$ and $\{\hat{\varphi}_{p,k}\}_{k\in\mathbb{N}^+}\subset L^2(\hat{\gamma})$ for the velocity and for the pressure, respectively. We introduce the HiMod reduced spaces

$$V_{m_u}=\left\{\mathbf{v}_{m_u}(x,\mathbf{y})=\sum_{k=1}^{m_u}\tilde{v}_k(x)\hat{\boldsymbol{\varphi}}_{u,k}(\psi_x(\mathbf{y})),\ \text{with } \tilde{v}_k\in V_{1D,u},\ \hat{\boldsymbol{\varphi}}_{u,k}\in V_{\hat{\gamma},u},\ x\in\Omega_{1D},\ \mathbf{y}\in\gamma_x\right\},$$
$$Q_{m_p}=\left\{q_{m_p}(x,\mathbf{y})=\sum_{s=1}^{m_p}\tilde{q}_s(x)\hat{\varphi}_{p,s}(\psi_x(\mathbf{y})),\ \text{with } \tilde{q}_s\in V_{1D,p},\ \hat{\varphi}_{p,s}\in V_{\hat{\gamma},p},\ x\in\Omega_{1D},\ \mathbf{y}\in\gamma_x\right\},$$

where $m_u$ and $m_p$ denote the number of modes related to the velocity and the pressure, respectively, $V_{1D,u}\subseteq[H^1_{\Gamma_{dir}}(\Omega_{1D})]^3$ and $V_{1D,p}\subseteq L^2(\Omega_{1D})$ are the 1D spaces associated with the supporting fiber $\Omega_{1D}$ for the velocity and the pressure, respectively, and with $V_{\hat{\gamma},u}=span\{\hat{\boldsymbol{\varphi}}_{u,k}\}$, $V_{\hat{\gamma},p}=span\{\hat{\varphi}_{p,s}\}$.

We introduce a uniform 1D grid $\mathcal{T}_h$ on $\Omega_{1D}$ and we associate with this partition the FE spaces $V^h_{1D,u}$, with $dim(V^h_{1D,u})=N_{h,u}$ and basis $\{\boldsymbol{\zeta}_{u,l}=[\zeta_{x,l},\zeta_{r,l},\zeta_{\vartheta,l}]^T\}_{l=1}^{N_{h,u}}$, and $V^h_{1D,p}$, with $dim(V^h_{1D,p})=N_{h,p}$ and basis $\{\zeta_{p,l}\}_{l=1}^{N_{h,p}}$.

Concerning the choice of the modal basis, it is a priori possible to use a different number of modes, $m_x$, $m_r$, $m_\vartheta$, $m_p$, for the three components of the velocity and for the pressure, with corresponding bases $\{\hat{\varphi}_{x,k}\}$, $\{\hat{\varphi}_{r,k}\}$, $\{\hat{\varphi}_{\vartheta,k}\}$, $\{\hat{\varphi}_{p,k}\}$. For the sake of simplicity, we assume $m_x=m_r=m_\vartheta=m_u$ and $\hat{\varphi}_{x,k}=\hat{\varphi}_{r,k}=\hat{\varphi}_{\vartheta,k}=\hat{\varphi}_k$. Analogously, we set $\zeta_{x,l}=\zeta_{r,l}=\zeta_{\vartheta,l}=\zeta_{u,l}$. Thus, the HiMod velocity and pressure are expanded as

$$\mathbf{u}^h_{m_u}(x,\mathbf{y})=\sum_{k=1}^{m_u}\sum_{i=1}^{N_{h,u}}\begin{bmatrix}u_{x,k,i}\\ u_{r,k,i}\\ u_{\vartheta,k,i}\end{bmatrix}\varphi_k(\psi_x(\mathbf{y}))\zeta_{u,i}(x),\quad p^h_{m_p}(x,\mathbf{y})=\sum_{w=1}^{m_p}\sum_{s=1}^{N_{h,p}}p_{w,s}\zeta_{p,s}(x)\hat{\varphi}_{p,w}(\psi_x(\mathbf{y})), \tag{15}$$

while the test functions are defined as $\mathbf{v}^h_{m_u}=[\zeta_{u,b}\hat{\varphi}_c,\zeta_{u,b}\hat{\varphi}_c,\zeta_{u,b}\hat{\varphi}_c]^T$ for $b=1,\dots,N_{h,u}$ and $c=1,\dots,m_u$, $q^h_{m_p}=\zeta_{p,l}\hat{\varphi}_{p,j}$ for $l=1,\dots,N_{h,p}$ and $j=1,\dots,m_p$. We refer to Appendix B for the explicit HiMod formulation of problem (14).




DOI: 10.1002/nme

**Remark** As well known, the choice of finite dimensional spaces for velocity and pressure must fulfill the *inf-sup condition* [28, 29]. While the issue is largely investigated for finite element and spectral methods [30, 31, 32, 16], we are not aware of any theoretical result for hybrid methods that involve both the techniques. We follow here an empirical approach, inspired by the finite element and the spectral theory. So we use piecewise quadratic velocity/linear pressure for the axial dependence (FE) and set $m_u = m_p + 2$ for the transverse one (spectral method). Other choices have been pursued in [8], with $m_u = 2m_p - 2$.

After the HiMod discretization of the generalized Stokes problem, the resulting matrix has a block structure with the following partitioning of degrees of freedom: $m_u N_{h,u}$ DOFs are associated with each component $u_x$, $u_r$ and $u_\vartheta$ of the velocity, whereas the remaining $m_p N_{h,p}$ degrees of freedom are related to the pressure. The outer block-structure couples the components of the velocity and the pressure, as it is standard for the Stokes problem. Then, each macro-block shares the typical block-wise pattern of the HiMod reduction applied to a scalar problem (see Figure 7).

In the implementation here adopted, the innermost loop assembles the FE component. Another choice stems from swapping the order of assembly. Although the two strategies of assembly are equivalent from a numerical viewpoint, the efficiency of the solver may vary, especially with a view to a parallel implementation of the method. This is an issue that is still under investigation [33].

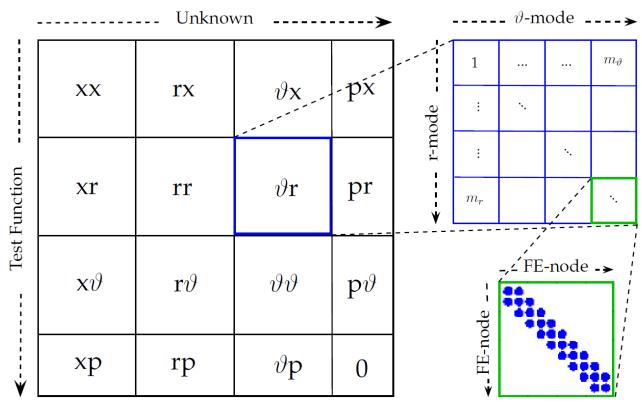


Figure 7. Block structure of the HiMod matrix associated with the generalized Stokes problem. The indices $x, r, \vartheta, p$ in each block highlight the coupling of the three components of the velocity with the pressure.

### *4.2. Steady case: Poiseuille flow*

We compare the performance of the top-down basis (5), solution to a 2D Sturm-Liouville eigenvalue problem, as opposed to the family of bottom-up basis functions of type (8). In particular, in view of the discussion carried out in Section 2.2.2, we select Chebyshev polynomials with quadratic shift to describe the radial component of the modal basis. For the sake of the comparison, we enforce homogeneous Dirichlet boundary conditions on $\Gamma_{lat}$.

Let $\Omega$ be a cylindrical domain with radius $R = 0.5$ and length $L_x = 6$. We solve the generalized Stokes equations (14) completed with the following boundary conditions:

$$\begin{cases} \mathbf{u} = \mathbf{0} & \text{on } \Gamma_{lat} \\ u_x = \dfrac{5}{L_x}\dfrac{(R^2 - r^2)}{4\mu} & \text{on } \Gamma_{in} \\ u_r = u_\vartheta = 0 & \text{on } \Gamma_{in} \\ (2\nu\mathbb{D} - p\mathbb{I})\mathbf{n}\cdot\mathbf{n} = 0 & \text{on } \Gamma_{out} \\ u_r = u_\vartheta = 0 & \text{on } \Gamma_{out}. \end{cases} \tag{16}$$

For $\alpha = 0$ (steady flow) we have the classical Poiseuille flow (see, e.g., [34]). The HiMod discretization here employed selects $m_u = 10$, $m_p = 8$ and a uniform mesh along $\Omega_{1D}$ of size $h = 0.125$.



DOI: 10.1002/nme

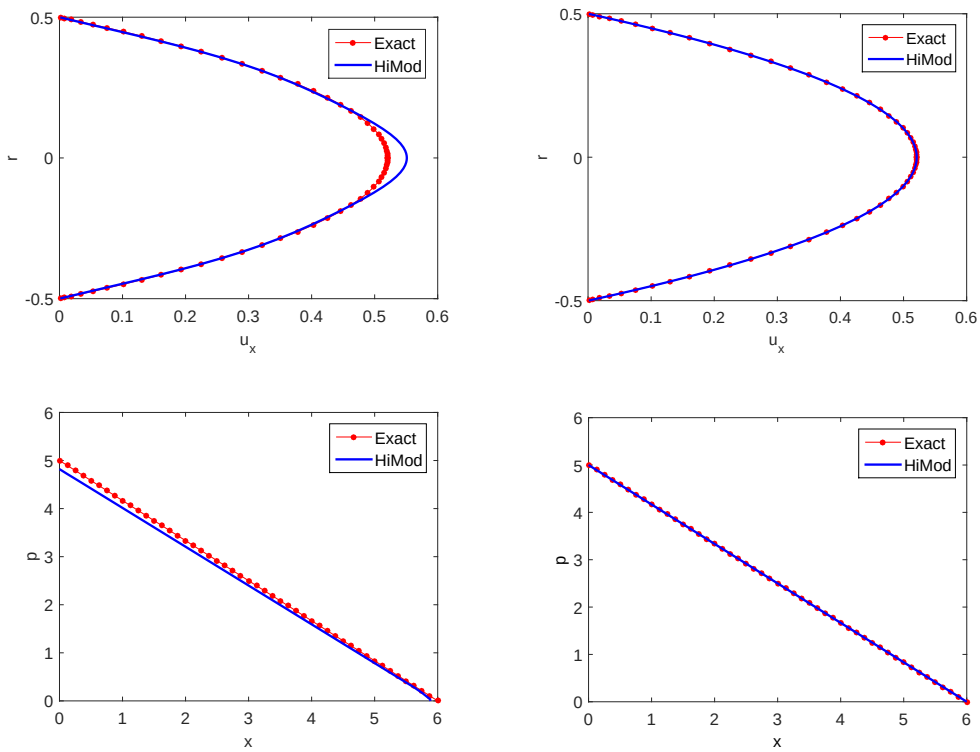


Figure 8. Poiseuille flow: Exact (dotted line) and HiMod (solid line) axial velocity at $x = L_x/3$ (top) and pressure drop (bottom) computed via a top-down (left) and a bottom-up (right) basis.

### *4.2.1. Top-down basis*

As shown in Figure 8 (top-left) the peak reached by the axial component of the HiMod velocity does not match the analytical profile and this mismatch increases moving towards the outflow. The pressure gradient, although constant as expected, is underestimated (see Figure 8 (bottom-left)). Nevertheless, the accuracy of the approximation can be enhanced by increasing the number of modes. Figure 9 (top) shows the trend of the $L^2(\Omega)$-norm of the relative error associated with the HiMod velocity and the pressure as a function of the modal index, for different values of $h$. Notice that, in such a case, a refinement of the mesh does not provide any improvement in the accuracy of the HiMod solution since both the velocity and the pressure belong to the discrete space associated with $\Omega_{1D}$. Hence, the global error is dominated by the modal error, which drops as the number of modal functions increases sufficiently. Therefore, Bessel functions are inefficient in the spirit of a HiMod reduction, where few transverse modes are expected to improve the accuracy of the approximation. Finally, it is worth noting that the number of degrees of freedom necessary to guarantee a fixed level of accuracy is consistently smaller for HiMod than for FEM or, equivalently, for a fixed size of the problem HiMod provides a more accurate solution than FEM (see Figure 9 (bottom)).

### *4.2.2. Bottom-up basis*

The radial basis polynomials obtained with the bottom-up approach (see Table II) do not vanish at the boundary. Therefore, they need to be artificially "educated" to match the boundary data, so that the resulting modal basis is consistent with the Parity Theorem. A basis that fulfils such a requirement is proposed in [35]. For all $j, n = 1, 2, \ldots$, we have

$$\begin{cases} \xi_n^E(r) = T_n(2r^2 - 1) - 1 & \text{if } j \text{ is even} \\ \xi_n^O(r) = rT_n(2r^2 - 1) - r & \text{if } j \text{ is odd.} \end{cases} \tag{17}$$




DOI: 10.1002/nme

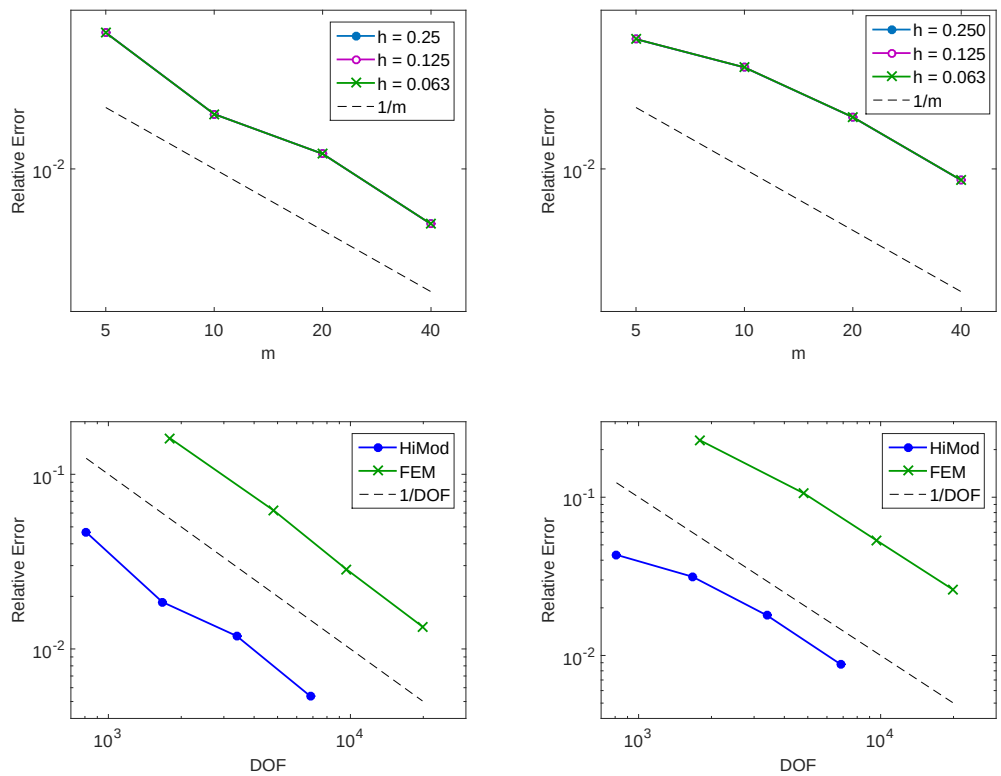


Figure 9. Poiseuille flow: $L^2(\Omega)$-norm of the HiMod relative error for the velocity (left) and for the pressure (right) for different modes and mesh sizes (top); Comparison between the $L^2(\Omega)$-norm of the relative error associated with HiMod and FEM (bottom) for the velocity (left) and the pressure (right).

| $k$ odd | | | | |
|---|---|---|---|---|
| $\cos(0\vartheta)$ | $\xi_1^E(r)$ (1) | $\xi_2^E(r)$ (3) | $\xi_3^E(r)$ (7) | $\xi_4^E(r)$ (13) |
| $\cos(1\vartheta)$ | $\xi_1^O(r)$ (5) | $\xi_2^O(r)$ (9) | $\xi_3^O(r)$ (15) | ... |
| $\cos(2\vartheta)$ | $\xi_1^E(r)$ (11) | $\xi_2^E(r)$ (17) | ... | |
| $\cos(3\vartheta)$ | $\xi_1^O(r)$ (19) | ... | | |

| $k$ even | | | | |
|---|---|---|---|---|
| $\sin(1\vartheta)$ | $\xi_1^O(r)$ (2) | $\xi_2^O(r)$ (4) | $\xi_3^O(r)$ (8) | $\xi_4^O(r)$ (14) |
| $\sin(2\vartheta)$ | $\xi_1^E(r)$ (6) | $\xi_2^E(r)$ (10) | $\xi_3^E(r)$ (16) | ... |
| $\sin(3\vartheta)$ | $\xi_1^O(r)$ (12) | $\xi_2^O(r)$ (18) | ... | |
| $\sin(4\vartheta)$ | $\xi_1^E(r)$ (20) | ... | | |

Table III. Ordering of the bottom-up basis functions $\{\hat{\varphi}_k\}$. The numbering refers to a triangular truncation, whereas a rectangular truncation employs the same number of radial basis functions for each angular frequency.

We order functions (17) as in Table III (see [35]), and we use a rectangular truncation. Concerning the reduction of the pressure, standard Chebyshev polynomials with quadratic shift are used, as no boundary condition is enforced on $p$.

As a consistency check, we notice that the quadratic solution for the axial component of the velocity belongs to the reduced space, and the Chebyshev polynomials compute it with a global relative error of the order of $10^{-7}$ (see Figure 8 (top-right)). This error is not improved by increasing



DOI: 10.1002/nme

the number of modes or reducing the FE mesh size. The same holds for the linear pressure, as shown in Figure 8 (bottom-right).

### *4.3. Unsteady case: Womersley flow*

HiMod can be generalized to unsteady problems with no particular technical issues. The generalized Stokes problem needs to be solved at each time step as the result of a standard time discretization. In particular, we solve the problem on the Womersley test case, the well known counterpart of Poiseuille profile with a time-periodic pressure drop between inlet and outlet [36]. More precisely, the pressure drop is given by $AL_x e^{i\omega t}$, with constant amplitude $A$, frequency $\omega = \frac{2\pi}{T}$ and period $T$ (the heart beat). The interplay between the oscillatory flow frequency $\omega$ and the effects of the kinematic viscosity $\nu$ is described by the Womersley number $\text{Wo} = R\sqrt{\omega/\nu}$. We reproduce here the test proposed in [8]. The amplitude and the period are set to $A = 1$ and $T = 1$ (i.e., $\omega = 2\pi$), respectively, while the length of the pipe and the radius are set to $L_x = 2$ and $R = 0.2$, respectively. We simulate the flow associated with different Womersley numbers, $\text{Wo} \in \{3, 5, 10, 20\}$, by varying the viscosity of the fluid. We simulate a complete period by choosing $\Delta t = \frac{T}{1000}$, and we assign Neumann conditions to enforce the pressure drop along the axial direction, homogeneous conditions for the transverse components of the velocity at the inlet/outlet and no-slip lateral conditions. The mesh size along the axis $\Omega_{1D}$ is $h = 0.125$, and the number of modes for the velocity is $m_u \in \{5, 9, 13\}$. The HiMod solution is compared to the analytical solution in Figure 10 at different times and for the different values of Wo. For low Womersley numbers, characterized by an oscillating profile very close to the Poiseuille parabolic solution, HiMod is accurate even with very few modes. As the Womersley number increases, the wave front flattens in the center of the pipe and only a higher number of transverse modes is able to guarantee accuracy. This is confirmed by the errors in Table IV. Indeed, the $L^2(\Omega)$-norm of the error is approximately constant independently of the number of modes for $\text{Wo} \in \{3, 5\}$, whereas it drops as $m_u$ increases, for $\text{Wo} \in \{10, 20\}$. Accordingly, the accuracy of the HiMod approximation is preserved for each value of the Womersley number only for a sufficiently large number of modes ($m_u = 13$). Furthermore, since the initial HiMod solution coincides with the exact solution, the error at $t = 0$ reduces to the HiMod truncation error. Figure 11 highlights the phase-lag between the (normalized) axial velocity and the oscillating (normalized) pressure on the centerline at the inlet for $\text{Wo} = 3$ and $m_u = 5$, in accordance with [36, 37]. It is evident that the HiMod solution tightly matches the analytical profile.

Note that the Womersley flow is an analytical solution not only to the unsteady Stokes problem, but also to the unsteady Navier-Stokes equations, since the nonlinear term vanishes for this choice of profile. The results presented here are obtained as the solution to problem (14). Nevertheless, the same tests were run by adding the nonlinear term, but no significant difference is detected and the error is essentially preserved. This allows us to compare the HiMod with the TEPEM numerical performance. In particular, we will refer to Table I in [8]. The level of accuracy obtained with $m_u$ HiMod transverse modes is guaranteed with approximately $m_u^2$ TEPEM modes, and with a time step four times larger than the one used in [8]. This is likely a consequence of the strict correspondence between the geometry and the HiMod basis, in contrast to the Cartesian map used in TEPEM. Indeed, this is easy to implement, but introduces a local lack of regularity that affects the convergence rate. A more systematic investigation of this point will be carried in the follow up of this work, focused on non-axisymmetric Navier-Stokes problems [10].

## 5. NUMERICAL TESTS IN NONTRIVIAL DOMAINS

We present some further numerical tests inspired by computational hemodynamics. The ultimate goal of HiMod in this field is to provide an efficient way for simulating blood flow in arteries with computational costs comparable to 1D models, yet preserving local accuracy in the transverse components. A first contribution in this direction is given in [8]. We demonstrate here that using the cylindrical coordinate framework on nontrivial axisymmetric geometries is efficient, even




DOI: 10.1002/nme

| | | $t\ [s]$ | | | |
|---|---|---|---|---|---|
| | | 0 | 0.10 | 0.25 | 0.40 |
| Wo = 3 | $m_u$=5 | 6.17e-7 | 7.12e-5 | 1.57e-4 | 1.40e-4 |
| | $m_u$=9 | 6.17e-7 | 7.12e-5 | 1.57e-4 | 1.40e-4 |
| | $m_u$=13 | 6.18e-7 | 7.12e-5 | 1.57e-4 | 1.40e-4 |
| Wo = 5 | $m_u$=5 | 5.19e-7 | 6.63e-5 | 2.13e-4 | 2.93e-4 |
| | $m_u$=9 | 4.22e-7 | 6.65e-5 | 2.14e-4 | 2.94e-4 |
| | $m_u$=13 | 4.22e-7 | 6.65e-5 | 2.14e-4 | 2.94e-4 |
| Wo = 10 | $m_u$=5 | 1.20e-4 | 2.02e-4 | 2.85e-4 | 4.09e-4 |
| | $m_u$=9 | 2.98e-7 | 5.94e-5 | 2.35e-4 | 3.80e-4 |
| | $m_u$=13 | 2.98e-7 | 5.94e-5 | 2.35e-4 | 3.80e-4 |
| Wo = 20 | $m_u$=5 | 1.59e-3 | 8.31e-4 | 1.75e-3 | 3.13e-3 |
| | $m_u$=9 | 2.21e-6 | 5.59e-5 | 2.44e-4 | 4.16e-4 |
| | $m_u$=13 | 2.09e-7 | 5.47e-5 | 2.45e-4 | 4.19e-4 |

Table IV. Womersley flow: $L^2(\Omega)$-norm of the error associated with the HiMod velocity for different Wo numbers and at different times.

though non-trivial from the implementation standpoint. Moreover, the HiMod solution to the Stokes problem outperforms the standard FEM in terms of computational costs, as already remarked in [8].

### *5.1. Vascular models*

We consider three types of non-trivial geometries that model the natural tapering of blood vessels, and the most common cardio-vascular diseases (stenoses and aneurysms).

**Tapered pipes** It has been noted by several authors that arteries feature tapering along their axis and that this has a significant impact on hemodynamics (and, consequently, on the design of grafts and prosthesis [38, 39, 40]). In a tapered pipe, the radius can be modeled as [41]

$$R(x) = -(\tan \Psi)x + R_{in},$$

where $\Psi = \frac{(R_{out}-R_{in})}{L_x}$ is the tapering angle, and with $R_{in}$ and $R_{out}$ the radius at the inflow and at the outflow section, respectively (see Figure 12 (top)).

**Aneurysmatic and stenotic vessels** An aneurysm is a balloon-like dilation in an arterial vessel (see Figure 12 (center) for a sketch). The growth and rupture of the bulge is related to hemodynamics factors, such as blood velocity, wall shear stress, pressure, particle residence time and flow impingement [42].

Arterial stenoses are local restrictions of the artery caused by localized plaques (see Figure 12 (bottom)). We model the radius for both the diseases as a quadratic exponential function of the axial variable, i.e., as

$$R(x) = R_0 + \kappa e^{-\left(x-\frac{L_x}{2}\right)^2}, \tag{18}$$

where $R_0$ is the radius of the inflow and of the outflow sections, while $\kappa$, with $\kappa \in [-1, 1]$, takes into account the entity of the occlusion or dilation. In particular, the parameter $\kappa$ is positive in the case of an aneurysm, negative for a stenosis.

In what follows we simulate the unsteady Stokes problem in a tapered pipe and in an aneurysmatic vessel ($\kappa = 0.5$). The case $\kappa < 0$ is omitted for the sake of brevity, the HiMod performances being comparable to the results shown here. A complete description of the results can be found in [20]. We enforce the same boundary conditions as for the Womersley test case, and we set the number of modes for the velocity and the mesh size along $\Omega_{1D}$ to $m_u = 10$ and $h = 0.125$, respectively.



DOI: 10.1002/nme

### 5.2. *HiMod approximation*

**Tapered pipes** The flow is driven by a space-dependent oscillating pressure gradient, such that the amplitude of the pressure oscillation dicreases along the $x$-axis (see Figure 13 (left)). Conversely, the oscillation of the Womersley velocity profile at the center of the inlet section of the pipe is magnified along the $x$-axis, so that the maximal oscillation is reached at the outlet section (see Figure 13 (right)). On each transverse section and at each time step, the $x$-component of the velocity reproduces the Womersley profile associated with the radius of the corresponding section $\gamma_x$, as shown in Figure 14 (top). Notice that the tapering of the domain triggers some transverse dynamics, in contrast to the Womersley flow in a cylindrical pipe with constant radius. Thus, the velocity is not purely axial, as for the case of constant radius. The presence of a radial component is correctly detected by the HiMod solution (see Figure 14 (center)). In particular, the planar components point inward as long as the peak of the axial velocity is positive. They turn outward as soon as the flow reverses. Finally, Figure 14 (bottom) shows the 3D HiMod approximation for four different times on the whole domain.

**Aneurysmatic vessels** At each time the pressure is linear along the $x$-axis in the inflow and outflow cylindrical segments, with an inflection point inside the aneurysm. In particular, it increases where the vessel enlarges, and it reduces where the regular lumen of the vessel is restored (see Figure 15 (left)). Conversely, the axial velocity on the centerline drops inside the bulge, due to the conservation of energy (see Figure 15 (right)). We refer to [20] for a detailed analysis of the effect of the size $\kappa$ of the aneurysm on the pressure and velocity profiles. The axial component of the velocity on each transverse section features the profile typical of the Womersley flow in a cylindrical pipe, as shown in Figure 16 (top). However, note that the flow develops a parabolic profile in the cylindrical segments (see, e.g., sections at $x = 0$, and $x = L_x/3$), whereas it flattens around $r = 0$ within the aneurysm (section at $x = L_x/2$). Moreover, differently from the proximal and distal profiles, no flow inversion takes place in the bulge, in the proximity of the wall (see Figure 16 (top-right)). The transverse components of the velocity are directed outward until the flow reverses at $t = 0.40s$ (see Figure 16 (center)). Finally, the 3D velocity profiles on different sections are shown in Figure 16 (bottom).

We stress that the transverse dynamics properly described in these results are out of reach for 1D models, while HiMod - that conceptually is a sort of 1D enriched modeling - is able to capture the local components of these dynamics by properly tuning the spectral discretization.

## 6. CONCLUSIONS

In this work we extended the Hierarchical Model Reduction to 3D cylindrical domains and to differential problems actually involved in haemodynamic modeling. While the application of HiMod to 2D or 3D slabs is straightforward thanks to the Cartesian tensor product, the cylindrical setting requires a specific analysis. First, we considered a standard ADR problem. The comparison between the HiMod solution and the corresponding 3D approximation highlights the competitiveness of HiMod with respect to FEM, both in terms of computational effort and accuracy of the approximation. When the number of transverse modes is sufficiently large, the HiMod approximation is fully comparable with the FE one, yet obtained with a much smaller number of unknowns. Then, we carried out the HiMod formulation for the generalized Stokes problem in cylindrical coordinates. The choice of the basis set and of the corresponding approximation properties in this case required a deeper discussion. The promising performances obtained with quadratic-shifted Chebyshev polynomials enabled us to move towards geometries more challenging for medical applications. In particular, we introduced elementary models for cardiovascular pathologies such as aneurysms or stenoses. The HiMod solutions match the expected results very well, for both steady and evolutionary models. In particular, the results on stenotic or aneurysmatic vessels confirm that a HiMod reduction is capable of detecting local transverse dynamics that are




DOI: 10.1002/nme

totally dropped by standard 1D models. This feature points out the role of the HiMod approach as a (cheap) "psychologically" 1D model, capable of improving the local accuracy. A similar coexistence of computational cost reduction and local accuracy is performed by the Geometrical Multiscale approach (see [43, 3, 44]). Nevertheless, the advantage of a HiMod reduction with respect to such a method is that the model is not dimensionally heterogeneous. Thus, the local refinement is by far easier to be obtained and managed in extended networks of pipes.

We plan to use this method for modeling networks of pipes [8], such as a significant portion of the arterial tree. Indeed, if, on the one hand, it has been shown that HiMod can introduce a significant computational saving compared to full 3D modeling, on the other hand one of the ultimate goals of the methodology is to provide an alternative to 1D Euler-based models. At this stage, we cannot perform an extensive comparison with 1D Euler models, since the latter is specifically designed for fluid-structure interaction, which is one of the follow-up of the present work. We are currently working on extending the HiMod reduction to the nonlinear Navier-Stokes equations in non-axisymmetric domains, which translates into a dependence of the radius not only on the axial but also on the angular coordinate [10]. Other open issues are the inf-sup condition for HiMod solvers and the identification of linear algebra solvers for the HiMod system, specifically designed for exploiting the sparsity pattern and the intrinsic nature of the method, such as multilevel techniques.

ACKNOWLEDGMENTS

The authors gratefully acknowledge support by the Computational and Life Sciences (CLS) Strategic Initiative of Emory University. This research was supported in part by US National Science Foundation Grant DMS-1419060. The financial support of GNCS-Project "Tecniche di riduzione della complessità computazionale per le scienze applicate" is also gratefully acknowledged by the second author.

# Appendices

## A. ADR HIMOD COEFFICIENTS

We denote the inverse transpose of the strain gradient tensor by

$$\hat{\mathbb{F}}^{-T} = \frac{\partial \hat{\boldsymbol{\psi}}}{\partial \mathbf{z}} \circ \hat{\boldsymbol{\psi}}^{-1} = \begin{bmatrix} 1 & -\dfrac{\hat{r}}{R}\dfrac{\partial R}{\partial \hat{x}} & 0 \\ 0 & \dfrac{1}{R} & 0 \\ 0 & -\dfrac{1}{R^2}\dfrac{\partial R}{\partial \hat{\vartheta}} & \dfrac{1}{R} \end{bmatrix} = \begin{bmatrix} 1 & \hat{D}_r & \hat{D}_\vartheta \\ 0 & \hat{J}_r & \hat{D}_{r\vartheta} \\ 0 & \hat{D}_{\vartheta r} & \hat{J}_\vartheta \end{bmatrix}, \tag{19}$$

where the subscripts $r$ and $\vartheta$ refer to the radial and angular component, respectively, while $\hat{r}$ and $\hat{\vartheta}$ denote the polar coordinates in the reference domain. Notice that, if we assume the physical radius $R$ to be constant, matrix (19) features a diagonal pattern, being $\hat{D}_r = \hat{D}_\vartheta = \hat{D}_{r\vartheta} = \hat{D}_{\vartheta r} = 0$ and $\hat{J}_r = \hat{J}_\vartheta = R^{-1}$.




DOI: 10.1002/nme

The coefficients of the HiMod formulation (11) for the ADR problem (9) with viscosity $\mu$, convective field $\mathbf{b} = [b_x, b_r, b_\vartheta]^T$, reaction coefficient $\sigma$ and forcing term $f$ are given by

$$\begin{aligned}
\mathfrak{a}_{kj} = \int_{\hat\gamma} \Bigg( & \mu(\hat D_r^2 + \hat D_{\vartheta r}^2 + \hat J_r^2)\frac{\partial\hat\varphi_k}{\partial\hat r}\frac{\partial\hat\varphi_j}{\partial\hat r} + \mu(\hat D_r\hat D_\vartheta + \hat J_r\hat D_{r\vartheta} + \hat D_{\vartheta r}\hat J_\vartheta)\frac{1}{\hat r}\frac{\partial\hat\varphi_k}{\partial\hat r}\frac{\partial\hat\varphi_j}{\partial\hat\vartheta} \\
& + \mu(\hat D_r\hat D_\vartheta + \hat D_{r\vartheta}\hat J_r + \hat J_\vartheta\hat D_{\vartheta r})\frac{1}{\hat r}\frac{\partial\hat\varphi_k}{\partial\hat\vartheta}\frac{\partial\hat\varphi_j}{\partial\hat r} + \mu\left(\hat D_\vartheta^2 + \hat D_{r\vartheta}^2 + \hat J_\vartheta^2\right)\frac{1}{\hat r^2}\frac{\partial\hat\varphi_k}{\partial\hat\vartheta}\frac{\partial\hat\varphi_j}{\partial\hat\vartheta} \\
& + (b_x\hat D_r + b_r\hat J_r + b_\vartheta\hat D_{\vartheta r})\frac{\partial\hat\varphi_k}{\partial\hat r}\hat\varphi_j + (b_x\hat D_\vartheta + b_r\hat D_{r\vartheta} + b_\vartheta\hat J_\vartheta)\frac{1}{\hat r}\frac{\partial\hat\varphi_k}{\partial\hat\vartheta}\hat\varphi_j + \sigma\hat\varphi_k\hat\varphi_j\Bigg)\hat J d\hat\gamma, \\
\mathfrak{b}_{kj} = \int_{\hat\gamma} \mu\left(\hat D_r\frac{\partial\hat\varphi_k}{\partial\hat r}\hat\varphi_j + \frac{\hat D_\vartheta}{\hat r}\frac{\partial\hat\varphi_k}{\partial\hat\vartheta}\hat\varphi_j\right)\hat J d\hat\gamma, \qquad & \mathfrak{d}_{kj} = \int_{\hat\gamma} \mu\hat\varphi_k\hat\varphi_j\hat J d\hat\gamma, \\
\mathfrak{c}_{kj} = \int_{\hat\gamma} \left(\mu\hat D_r\hat\varphi_k\frac{\partial\hat\varphi_j}{\partial\hat r} + \mu\frac{\hat D_\vartheta}{\hat r}\hat\varphi_k\frac{\partial\hat\varphi_j}{\partial\hat\vartheta} + b_x\hat\varphi_k\hat\varphi_j\right)\hat J d\hat\gamma, \qquad & \mathfrak{f}_j = \int_{\hat\gamma} f(\hat{\boldsymbol\psi}^{-1}(\hat z))\hat\varphi_j\hat J d\hat\gamma,
\end{aligned}$$

being $\hat J = |\det(\hat{\mathbb{F}}^{-T})|$, and with $d\hat\gamma = \hat r d\hat r d\hat\vartheta$. The diagonal pattern of matrix $\hat{\mathbb{F}}^{-T}$ for the cylindrical setting with a constant radius yields some simplifications, so that

$$\begin{aligned}
\mathfrak{a}_{kj} &= \int_{\hat\gamma} \left(\frac{\mu}{R^2}\frac{\partial\hat\varphi_k}{\partial\hat r}\frac{\partial\hat\varphi_j}{\partial\hat r} + \frac{\mu}{R^2\hat r^2}\frac{\partial\hat\varphi_k}{\partial\hat\vartheta}\frac{\partial\hat\varphi_j}{\partial\hat\vartheta} + \frac{b_r}{R}\frac{\partial\hat\varphi_k}{\partial\hat r}\hat\varphi_j + \frac{b_\vartheta}{R\hat r}\frac{\partial\hat\varphi_k}{\partial\hat\vartheta}\hat\varphi_j + \sigma\hat\varphi_k\hat\varphi_j\right)\hat J d\hat\gamma, \\
\mathfrak{b}_{kj} &= 0, \quad \mathfrak{c}_{kj} = \int_{\hat\gamma} b_x\hat\varphi_k\hat\varphi_j\hat J d\hat\gamma, \quad \mathfrak{d}_{kj} = \int_{\hat\gamma} \mu\hat\varphi_k\hat\varphi_j\hat J d\hat\gamma, \quad \mathfrak{f}_j = \int_{\hat\gamma} f(\hat{\boldsymbol\psi}^{-1}(\hat z))\hat\varphi_j\hat J d\hat\gamma.
\end{aligned}$$

## B. GENERALIZED STOKES HIMOD COEFFICIENTS

The HiMod formulation of the generalized Stokes problem reads as:

For all $k = 1, \dots, m_u$, $w = 1, \dots, m_p$, $i = 1, \dots, N_{h,u}$, $q = 1, \dots, N_{h,p}$, find $u_{x,k,i}$, $u_{r,k,i}$, $u_{\vartheta,k,i}$, $p_{w,q}$ such that, $\forall b \in \{x, r, \vartheta, p\}$, $\forall j = 1, \dots, \{m_u, m_p\}$, $\forall l = 1, \dots, \{N_{h,u}, N_{h,p}\}$*

$$\begin{aligned}
\sum_{a\in\{x,r,\vartheta\}}\sum_{k=1}^{m_u}\sum_{w=1}^{m_p}\int_{\hat\Omega_{1D}} \Bigg\{ & \sum_{i=1}^{N_{h,u}} \left[\mathfrak{a}_{ab,kj}\zeta_{a,i}\zeta_{b,l} + \mathfrak{b}_{ab,kj}\zeta_{a,i}\zeta'_{b,l} + \mathfrak{c}_{ab,kj}\zeta'_{a,i}\zeta_{b,l} + \mathfrak{d}_{ab,kj}\zeta'_{a,i}\zeta'_{b,l}\right] u_{a,k,i} + \\
& \sum_{q=1}^{N_{h,p}} \left[\mathfrak{a}_{pb,wj}\zeta_{p,q}\zeta_{b,l} + \mathfrak{b}_{pb,wj}\zeta_{p,q}\zeta'_{b,l}\right] p_{w,q}\Bigg\} d\hat x = \int_{\hat\Omega_{1D}}\int_{\hat\gamma} \hat f\hat\varphi_{b,j}\zeta_{b,l}\hat J d\hat\gamma d\hat x,
\end{aligned} \tag{20}$$

where $\hat J = |\det(\hat{\mathbb{F}}^{-T})|$, $d\hat\gamma = \hat r d\hat r d\hat\vartheta$, and the coefficients $\mathfrak{a}_{ab,kj}$, $\mathfrak{a}_{pb,wj}$, $\mathfrak{b}_{ab,kj}$, $\mathfrak{b}_{pb,wj}$, $\mathfrak{c}_{ab,kj}$, $\mathfrak{d}_{ab,kj}$ collect the contribution of the transverse dynamics.

For the sake of simplicity, the following notation is adopted:

$$\begin{aligned}
& \mathcal{I}_{ab,cd}^{\alpha\beta,\gamma\delta}(f_1, f_2, \dots; \eta_1, \eta_2, \dots) = \\
& \qquad \int_{\hat\gamma} \left(\eta_1\eta_2\dots f_1(\hat J_r, \hat D_r, \hat D_\vartheta) f_2(\hat J_r, \hat D_r, \hat D_\vartheta)\dots {\varphi_{ac}}^{(\alpha,\beta)}(\hat r, \hat\vartheta){\varphi_{bd}}^{(\gamma,\delta)}(\hat r, \hat\vartheta)\right)\hat J d\hat\gamma,
\end{aligned} \tag{21}$$

where $\{a, b\} \in \{x, r, \vartheta; p\}$ refer to the component of the modal function, and $\{c, d\} \in \{1, \dots, m_u$ or $m_p\}$ are the corresponding modal indices. The superscripts $\{\alpha, \beta, \gamma, \delta\} \in \{0, 1\}$ take

*If $b = p$, the indices $j$ and $l$ run up to $m_p$ and $N_{h,p}$, respectively, and up to $m_u$ and $N_{h,u}$ otherwise.




DOI: 10.1002/nme

into account the differentiation applied to the modal basis. In particular, when $\alpha$ or $\gamma$ ($\beta$ or $\delta$) are set to 1, the corresponding modal function is differentiated with respect to the radial (angular) variable. Finally, $f_i$ is a function of $\hat{x}, \hat{r}, \hat{\vartheta}$ through $\hat{J}_r, \hat{D}_r, \hat{D}_\vartheta$, and $\eta_i \in \{\alpha, \nu, 2\nu, \pm 1\}$ are constant parameters. For instance,

$$\mathfrak{a}_{\vartheta x,sj} = \mathcal{I}^{10,01}_{\vartheta x,sj}\left(\hat{D}_r, \frac{\hat{J}_\vartheta}{\hat{r}}; \nu\right) = \int_{\hat{\gamma}} \left(\nu \hat{D}_r \frac{\hat{J}_\vartheta}{\hat{r}} \varphi_{\vartheta s}{}^{(1,0)}(\hat{r}, \hat{\vartheta}) \varphi_{xj}{}^{(0,1)}(\hat{r}, \hat{\vartheta})\right) \hat{J} d\hat{\gamma}.$$

The explicit expression for all the coefficients is provided below. Within each group, the coefficients are ordered by subscripts.

$$\begin{aligned}
\mathfrak{a}_{xx,kj} = {} & \mathcal{I}^{10,10}_{xx,kj}\left(\hat{D}_r^2; 2\nu\right) + \mathcal{I}^{00,00}_{xx,kj}(1;\alpha) + \mathcal{I}^{01,01}_{xx,kj}\left(\frac{\hat{J}_\vartheta^2}{\hat{r}^2}; \nu\right) + \mathcal{I}^{10,10}_{xx,kj}\left(\hat{J}_r^2; \nu\right), \\
\mathfrak{a}_{xr,kl} = {} & \mathcal{I}^{10,10}_{xr,kl}\left(\hat{D}_r, \hat{J}_r; \nu\right), \qquad \mathfrak{a}_{x\vartheta,kz} = \mathcal{I}^{01,10}_{x\vartheta,kz}\left(\hat{D}_r, \frac{\hat{J}_\vartheta}{\hat{r}}; \nu\right), \qquad \mathfrak{a}_{xp,ki} = \mathcal{I}^{10,00}_{xp,ki}\left(\hat{D}_r; -1\right), \\
\mathfrak{a}_{rr,hl} = {} & \mathcal{I}^{10,10}_{rr,hl}\left(\hat{D}_r^2; \nu\right) + \mathcal{I}^{00,00}_{rr,hl}(1;\alpha) + \mathcal{I}^{00,00}_{rr,hl}\left(\frac{\hat{J}_\vartheta^2}{\hat{r}^2}; 2\nu\right) + \mathcal{I}^{01,01}_{rr,hl}\left(\frac{\hat{J}_\vartheta^2}{\hat{r}^2}; \nu\right) + \mathcal{I}^{10,10}_{rr,hl}\left(\hat{J}_r^2; 2\nu\right), \\
\mathfrak{a}_{r\vartheta,hz} = {} & \mathcal{I}^{00,01}_{r\vartheta,hz}\left(\frac{\hat{J}_\vartheta^2}{\hat{r}^2}; 2\nu\right) + \mathcal{I}^{01,10}_{r\vartheta,hz}\left(\hat{J}_r, \frac{\hat{J}_\vartheta}{\hat{r}}; \nu\right) + \mathcal{I}^{01,00}_{r\vartheta,hz}\left(\frac{\hat{J}_\vartheta^2}{\hat{r}^2}; -\nu\right), \\
\mathfrak{a}_{rx,hj} = {} & \mathcal{I}^{10,10}_{rx,hj}\left(\hat{J}_r, \hat{D}_r; \nu\right), \qquad \mathfrak{a}_{rp,hi} = \mathcal{I}^{00,00}_{rp,hi}\left(-\frac{\hat{J}_\vartheta}{\hat{r}}; 1\right) + \mathcal{I}^{10,00}_{rp,hi}\left(-\hat{J}_r; 1\right), \\
\mathfrak{a}_{\vartheta\vartheta,sz} = {} & \mathcal{I}^{10,10}_{\vartheta\vartheta,sz}\left(\hat{D}_r^2; \nu\right) + \mathcal{I}^{00,00}_{\vartheta\vartheta,sz}(1;\alpha) + \mathcal{I}^{00,00}_{\vartheta\vartheta,sz}\left(\frac{\hat{J}_\vartheta^2}{\hat{r}^2}; \nu\right) + \mathcal{I}^{01,01}_{\vartheta\vartheta,sz}\left(\frac{\hat{J}_\vartheta^2}{\hat{r}^2}; 2\nu\right) + \\
& \mathcal{I}^{10,10}_{\vartheta\vartheta,sz}\left(\hat{J}_r^2; \nu\right) + \mathcal{I}^{10,00}_{\vartheta\vartheta,sz}\left(\hat{J}_r, \frac{\hat{J}_\vartheta}{\hat{r}}; -\nu\right) + \mathcal{I}^{00,10}_{\vartheta\vartheta,sz}\left(\hat{J}_r, \frac{\hat{J}_\vartheta}{\hat{r}}; -\nu\right), \\
\mathfrak{a}_{\vartheta r,sl} = {} & \mathcal{I}^{01,00}_{\vartheta r,sl}\left(\frac{\hat{J}_\vartheta^2}{\hat{r}^2}; 2\nu\right) + \mathcal{I}^{10,01}_{\vartheta r,sl}\left(\hat{J}_r, \frac{\hat{J}_\vartheta}{\hat{r}}; \nu\right) + \mathcal{I}^{00,01}_{\vartheta r,sl}\left(\frac{\hat{J}_\vartheta^2}{\hat{r}^2}; -\nu\right), \\
\mathfrak{a}_{\vartheta x,sj} = {} & \mathcal{I}^{10,01}_{\vartheta x,sj}\left(\hat{D}_r, \frac{\hat{J}_\vartheta}{\hat{r}}; \nu\right), \qquad \mathfrak{a}_{\vartheta p,si} = \mathcal{I}^{01,00}_{\vartheta p,si}\left(\frac{\hat{J}_\vartheta}{\hat{r}}; -1\right), \qquad \mathfrak{a}_{p\vartheta,wz} = \mathcal{I}^{00,01}_{p\vartheta,wz}\left(\frac{\hat{J}_\vartheta}{\hat{r}}; -1\right), \\
\mathfrak{a}_{px,wj} = {} & \mathcal{I}^{00,10}_{px,wj}\left(\hat{D}_r; -1\right), \qquad \mathfrak{a}_{pr,wl} = \mathcal{I}^{00,10}_{pr,wl}\left(\hat{J}_r; -1\right) + \mathcal{I}^{00,00}_{pr,wl}\left(\frac{\hat{J}_\vartheta}{\hat{r}}; -1\right);
\end{aligned}$$

$$\begin{aligned}
& \mathfrak{b}_{xx,kj} = \mathcal{I}^{10,00}_{xx,kj}\left(\hat{D}_r; 2\nu\right), \qquad \mathfrak{b}_{xr,kl} = \mathcal{I}^{10,00}_{xr,kl}\left(\hat{J}_r; \nu\right), \qquad \mathfrak{b}_{x\vartheta,kz} = \mathcal{I}^{01,00}_{x\vartheta,kz}\left(\frac{\hat{J}_\vartheta}{\hat{r}}; \nu\right), \\
& \mathfrak{b}_{xp,ki} = \mathcal{I}^{00,00}_{xp,ki}(1;-1), \qquad \mathfrak{b}_{rr,hl} = \mathcal{I}^{10,00}_{rr,hl}\left(\hat{D}_r; \nu\right), \qquad \mathfrak{b}_{\vartheta\vartheta,sz} = \mathcal{I}^{10,00}_{\vartheta\vartheta,sz}\left(\hat{D}_r; \nu\right), \\
& \mathfrak{b}_{px,wj} = \mathcal{I}^{00,00}_{px,wj}(1;-1);
\end{aligned}$$

$$\begin{aligned}
& \mathfrak{c}_{xx,kj} = \mathcal{I}^{00,10}_{xx,kj}\left(\hat{D}_r; 2\nu\right), \qquad \mathfrak{c}_{rr,rl} = \mathcal{I}^{00,10}_{rr,hl}\left(\hat{D}_r; \nu\right), \\
& \mathfrak{c}_{\vartheta\vartheta,sz} = \mathcal{I}^{00,10}_{\vartheta\vartheta,sz}\left(\hat{D}_r; \nu\right), \qquad \mathfrak{c}_{rx,hj} = \mathcal{I}^{00,10}_{rx,hj}\left(\hat{J}_r; \nu\right), \qquad \mathfrak{c}_{\vartheta x,sj} = \mathcal{I}^{00,01}_{\vartheta x,sj}\left(\frac{\hat{J}_\vartheta}{\hat{r}}; \nu\right), \\
& \mathfrak{d}_{rr,hl} = \mathcal{I}^{00,00}_{rr,hl}(1;\nu), \qquad \mathfrak{d}_{\vartheta\vartheta,sz} = \mathcal{I}^{00,00}_{\vartheta\vartheta,sz}(1;\nu), \qquad \mathfrak{d}_{xx,kj} = \mathcal{I}^{00,00}_{xx,kj}(1;2\nu).
\end{aligned}$$




DOI: 10.1002/nme

REFERENCES


1. Perotto S, Ern A, Veneziani A. Hierarchical local model reduction for elliptic problems: a domain decomposition approach. *Multiscale Modeling & Simulation* 2010; **8**(4):1102–1127.
2. Perotto S, Veneziani A. Coupled model and grid adaptivity in hierarchical reduction of elliptic problems. *Journal of Scientific Computing* 2014; **60**(3):505–536.
3. Formaggia L, Quarteroni A, Veneziani A. Multiscale models of the vascular system. *Cardiovascular Mathematics: Modeling and Simulation of the Circulatory System*, *MS&A - Modeling Simulation and Applications*, vol. 1, Formaggia L, Quarteroni A, Veneziani A (eds.). chap. 11, Springer Milan, 2009; 395–446, doi:10.1007/978-88-470-1152-6.
4. LeVeque R. *Numerical Methods for Conservation Laws*. Lectures in Mathematics ETH Zürich, Department of Mathematics Research Institute of Mathematics, Birkhäuser Basel, 1992.
5. Ern A, Perotto S, Veneziani A. Hierarchical model reduction for advection-diffusion-reaction problems. *Numerical Mathematics and Advanced Applications*, Kunish K, Günther O, Steinbach O (eds.). Numerical Mathematics and Advanced Applications, Springer: Berlin, Heidelberg, 2008; 703–710.
6. Perotto S, Zilio A. Hierarchical model reduction: three different approaches. *Numerical Mathematics and Advanced Applications 2011*. Springer, 2013; 851–859.
7. Aletti M, Perotto S, Veneziani A. Educated bases for the himod reduction of advection-diffusion-reaction problems with general boundary conditions. *Technical Report*, MOX Report No. 37/2015.
8. Blanco P, Alvarez LM, Feijóo R. Hybrid element-based approximation for the Navier–Stokes equations in pipe-like domains. *Computer Methods in Applied Mechanics and Engineering* 2015; **283**:971–993.
9. Blanco PJ, Watanabe SM, Queiroz RAB, Trenhago PR, Fernandes LG, Feijóo RA. Trends in the computational modeling and numerical simulation of the cardiovascular system. *Scientific Computing Applied to Medicine and Healthcare*, Feijóo RA, Ziviani A, Blanco PJ (eds.). chap. 2, 2012; 29–77.
10. Guzzetti S, Perotto S, Veneziani A. Hierarchical model reduction for hemodynamics applications. In preparation.
11. Perotto S. Hierarchical model (hi-mod) reduction in non-rectilinear domains. *Domain Decomposition Methods in Science and Engineering XXI*, Erhel J, Gander MJ, Halpern L, Pichot G, Sassi T, Widlund O (eds.). Springer International Publishing: Cham, 2014; 477–485, doi:10.1007/978-3-319-05789-7_45. URL `http://dx.doi.org/10.1007/978-3-319-05789-7_45`.
12. Perotto S, Reali A, Rusconi P, Veneziani A. HIGAMod: A Hierarchical IsoGeometric Approach for MODel reduction in curved pipes. *Computers & Fluids* 2016; doi:http://dx.doi.org/10.1016/j.compfluid.2016.04.014.
13. Brezis H. *Functional Analysis, Sobolev Spaces and Partial Differential Equations*. Universitext, Springer New York, 2011.
14. Courant R, Hilbert D. *Methods of Mathematical Physics*, vol. I. John Wiley & Sons, Inc.: New York, 1966.
15. Salsa S. *Equazioni a Derivate Parziali - Metodi, Modelli e Applicazioni*. 2nd edn., UNITEXT, Springer-Verlag Italia: Milano, 2010.
16. Canuto C, Hussaini MY, Quarteroni A, Zang TA. *Spectral Methods - Fundamentals in Single Domains*. Scientific Computation, Springer-Verlag: Berlin, Heidelberg, 2006.
17. Zhang S, Jin J. *Computation of Special Functions*. John Wiley and Sons, Inc.: New York, 1996.
18. Spiegel MR. *Theory and Problems of Fourier Analysis with Applications to Boundary Value Problems*. Schaum's Outline Series, McGraw-Hill: New York, 1974.
19. Davis HF. *Fourier Series and Orthogonal Functions*. Dover Publications: New York, 2012.
20. Guzzetti S. Hierarchical model reduction for incompressible flows in cylindrical domains. Master's Thesis, Politecnico di Milano, Italy 2014.
21. Rummler B. The eigenfunctions of the Stokes operator in special domains. I. *ZAMM-Journal of Applied Mathematics and Mechanics* 1997; **77**(8):619–627.
22. Boyd JP, Flyer N. Compatibility conditions for time-dependent partial differential equations and the rate of convergence of Chebyshev and Fourier spectral methods. *Computer Methods in Applied Mechanics and Engineering* 1999; **175**(3-4):281–309.
23. Stein EM, Shakarchi R. *Fourier Analysis: An Introduction*, *Princeton Lectures in Analysis*, vol. 1. Princeton Unversity Press: Princeton, New Jersey, 2003.
24. Boyd JP. *Chebyshev and Fourier Spectral Methods*. Second edn., Dover Publications: New York, 2001.
25. Gottlieb D, Orszag SA. *Numerical Analysis of Spectral Methods: Theory and Applications*. CBMS-NSF Regional Conference Series in Applied Mathematics, 1977.
26. Boyd JP, Yu F. Comparing seven spectral methods for interpolation and for solving the Poisson equation in a disk: Zernike polynomials, Logan–Shepp ridge polynomials, Chebyshev–Fourier series, cylindrical Robert functions, Bessel–Fourier expansions, square-to-disk conformal mapping and radial basis functions. *Journal of Computational Physics* 2011; **230**(4):1408–1438.
27. Costa MA, Simon DI. Molecular basis of restenosis and drug-eluting stents. *Circulation* 2005; **111**(17):2257–2273.
28. Brezzi F. On the existence, uniqueness and approximation of saddle-point problems arising from Lagrangian multipliers. *ESAIM: Mathematical Modelling and Numerical Analysis - Modélisation Mathématique et Analyse Numérique* 1974; **8**(R2):129–151.
29. Boffi D, Brezzi F, Fortin M, *et al.*. *Mixed Finite Flement Methods and Applications*, vol. 44. Springer, 2013.
30. Brenner S, Scott R. *The Mathematical Theory of Finite Element Methods*, vol. 15. Springer Science & Business Media, 2007.
31. Ern A, Guermond JL. *Theory and Practice of Finite Elements*, vol. 159. Springer Science & Business Media, 2013.
32. Quarteroni A, Valli A. *Numerical Approximation of Partial Differential Equations*, *Springer Series in Computational Mathematics*, vol. 23. 1994.
33. Barone A. Parallel and Multilevel Techniques for Hierarchical Model Reduction. Master's Thesis, Politecnico di Milano, Italy 2014.
34. Durst F. *Fluid Mechanics: An Introduction to the Theory of Fluid Flows*. Springer Berlin Heidelberg, 2008.





DOI: 10.1002/nme

35. Atkinson K, Hansen O. A spectral method for the eigenvalue problem for elliptic equations. *Electronic Transactions on Numerical Analysis* 2010; **37**:386–412.
36. Womersley JR. Method for the calculation of velocity, rate of flow and viscous drag in arteries when the pressure gradient is known. *The Journal of Physiology* 1955; **127**(3):553–563.
37. Hale JF, McDonald DA, Womersley JR. Velocity profiles of oscillating arterial flow, with some calculations of viscous drag and the Reynolds number. *The Journal of physiology* 1955; **128**(3):629–640.
38. Dwivedi AP, Pal TS, Rakesh L. Micropolar fluid model for blood flow through a small tapered tube. *Indian Journal of Technology* 1982; **20**:295–299.
39. Chaturani P, Pralhad RN. Blood flow in tapered tubes with biorheological applications. *Biorheology* 1985; **22**(4):303–314.
40. How TV, Black RA. Pressure losses in non-Newtonian flow through rigid wall tapered tubes. *Biorheology* 1987; **24**(3):337–351.
41. Sankar D, Hemalatha K. Non-linear mathematical models for blood flow through tapered tubes. *Applied Mathematics and Computation* 2007; **188**(1):567–582.
42. Samady H, Eshtehardi P, McDaniel MC, Suo J, Dhawan SS, Maynard C, Timmins LH, Quyyumi AA, Giddens DP. Coronary Artery Wall Shear Stress Is Associated With Progression and Transformation of Atherosclerotic Plaque and Arterial Remodeling in Patients With Coronary Artery DiseaseClinical Perspective. American Heart Association, Inc., 2011; 779–788, doi:10.1161/CIRCULATIONAHA.111.021824. URL `http://circ.ahajournals.org/content/124/7/779`.
43. Formaggia L, Nobile F, Quarteroni A, Veneziani A. Multiscale modelling of the circulatory system: a preliminary analysis. *Computing and Visualization in Science* 1999; **2**(2-3):75–83.
44. Mauri L, Perotto S, Veneziani A. Adaptive geometrical multiscale modeling for hydrodynamic problems. *Numerical Mathematics and Advanced Applications 2011*. Springer, 2013; 723–730.





DOI: 10.1002/nme

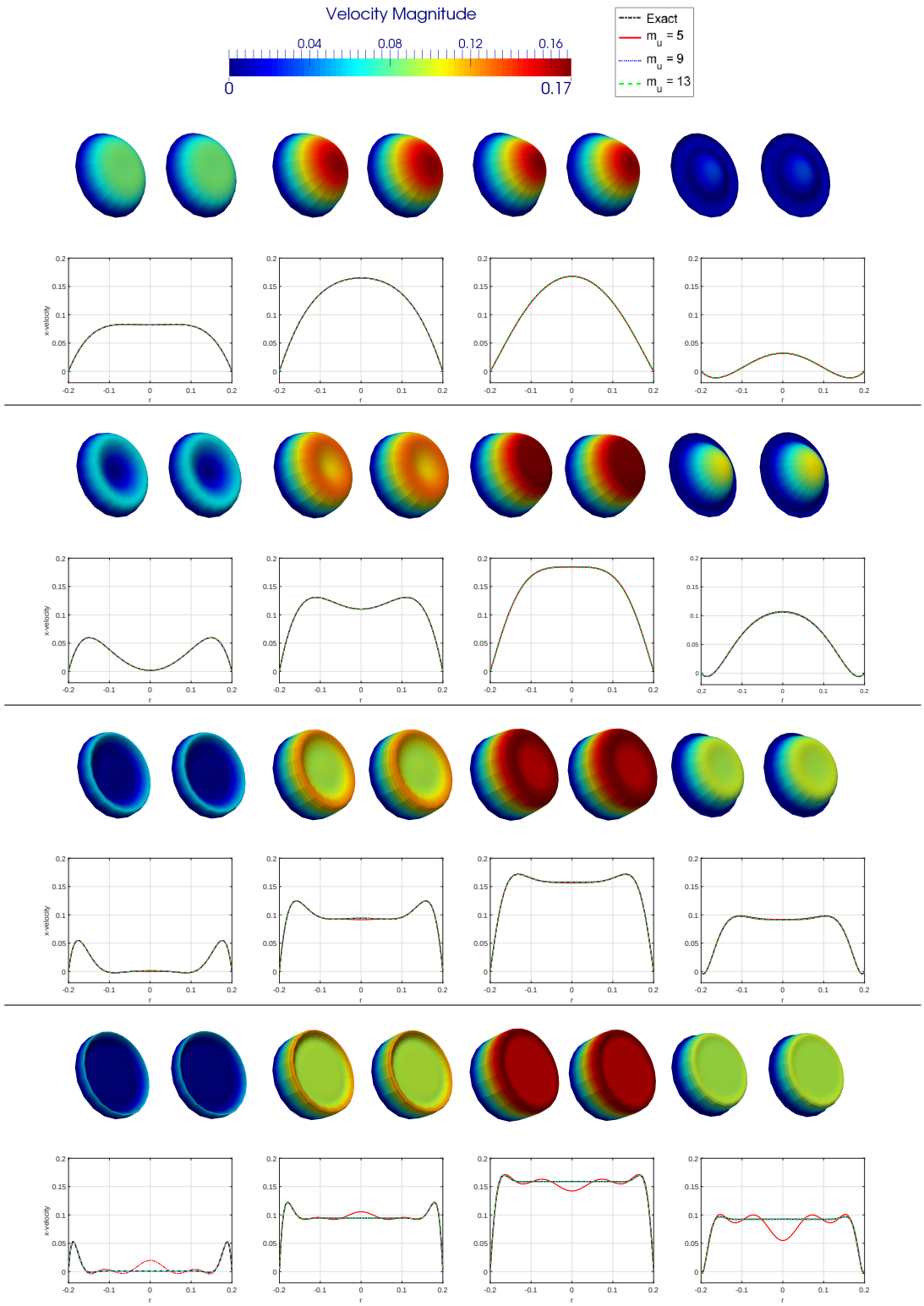


(a) $t = 0s$ (b) $t = 0.10s$ (c) $t = 0.25s$ (d) $t = 0.40s$

Figure 10. Womersley flow in a cylindrical pipe: In each panel velocity (top) and axial component (bottom) profile for the exact (left and dot-dashed line) and the HiMod (right and dotted, dashed, solid lines) solution at $x = L_x/2$ at different times for Wo $= 3, 5, 10, 20$ (top-bottom). The solid line corresponds to $m_u = 5$.




DOI: 10.1002/nme

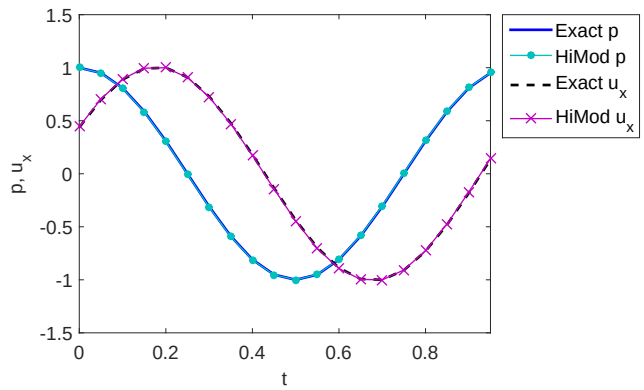


Figure 11. Womersley flow in a cylindrical pipe: Normalized exact (solid line) and HiMod (dotted line) pressure, normalized exact (dashed line) and HiMod ($\times$) axial velocity on the centerline at the inlet for $\mathrm{Wo} = 3$, $m_u = 5$.

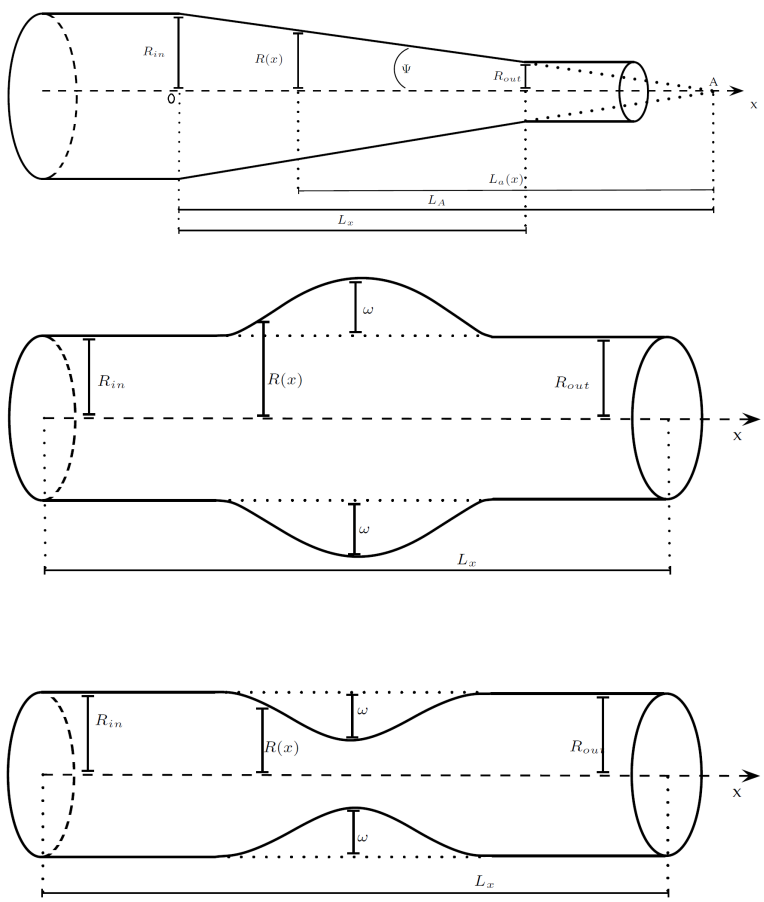


Figure 12. Sketch of a tapered pipe (top), of an aneurysmatic (center) and of a stenotic (bottom) vessel.




DOI: 10.1002/nme

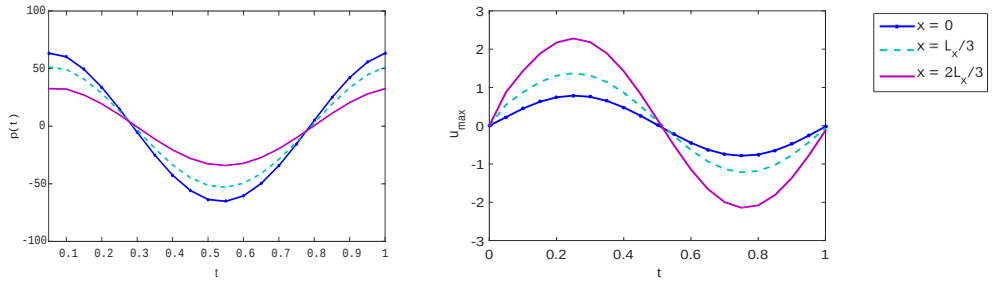


Figure 13. Womersley-like flow in a tapered pipe: Oscillating pressure (left) and centerline velocity (right) at $x = 0$ (dotted line), $x = L_x/3$ (dashed line), and $x = 2L_x/3$ (solid line).

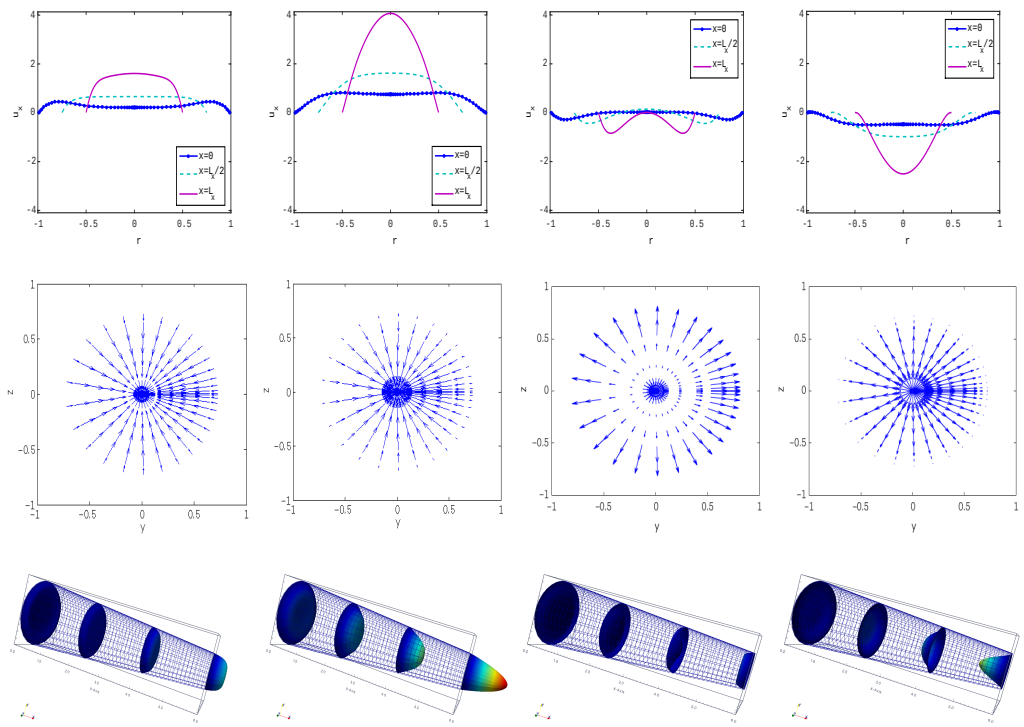


(a) $t = 0.05s$ (b) $t = 0.30s$ (c) $t = 0.45s$ (d) $t = 0.90s$

Figure 14. Womersley-like flow in a tapered pipe: Axial velocity at $x = 0$ (dotted line), $x = L_x/2$ (dashed line), and $x = L_x$ (solid line) (top); Radial velocity at $x = L_x/3$ (center) and 3D HiMod velocity profile (bottom) at different times.




DOI: 10.1002/nme

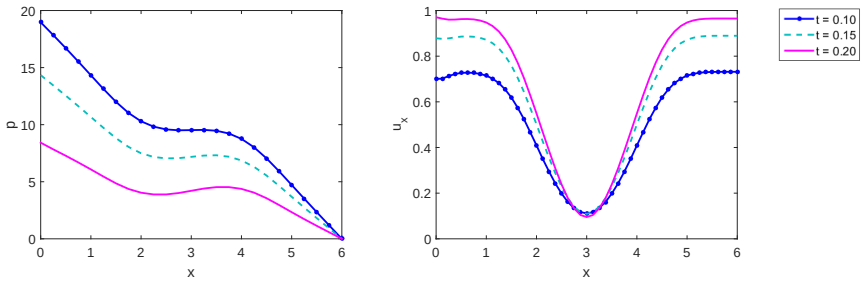


Figure 15. Womersley-like flow in an aneurysmatic pipe: Pressure (left) and axial velocity on the centerline (right) along the $x$-axis at $t = 0.10s$ (dotted line), $t = 0.15s$ (dashed line), and $t = 0.20s$ (solid line).

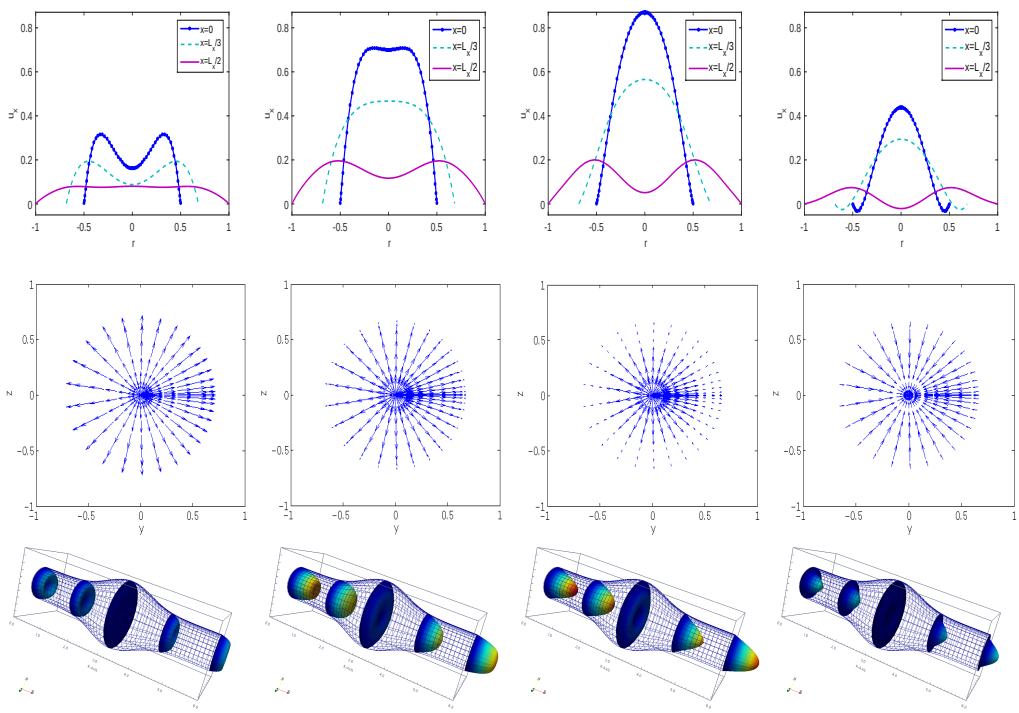


(a) $t = 0.00s$ (b) $t = 0.15s$ (c) $t = 0.30s$ (d) $t = 0.40s$

Figure 16. Womersley-like flow in an aneurysmatic vessel: Axial velocity at $x = 0$ (dotted line), $x = L_x/3$ (dashed line) and $x = L_x/2$ (solid line) sections (top); Radial velocity at $x = L_x/3$ (center); 3D HiMod velocity profile at different times (bottom).




DOI: 10.1002/nme